Supporting Information

Eliminating redox-mediated electron transfer mechanisms on molecular catalysts enables CO_2 conversion to ethanol

Authors: Maryam Abdinejad*[1]†, Amirhossein Farzi[2]†, Robin Möller-Gulland[1]†, Fokko Mulder[1], Chengyu Liu,[3] Junming Shao,[3] Marc Robert,[3,4] Ali Seifitokaldani*[2], Thomas Burdyny*[1]

Affiliations:
[1]Department of Chemical Engineering, Delft University of Technology; Delft, the Netherlands
[2]Department of Chemical Engineering, McGill University; Montreal, Montréal, Québec H3A 0C5, Canada
[3]Université Paris Cité, Laboratoire d'Electrochimie Moléculaire, CNRS, F-75006, Paris, France
[4]Institut Universitaire de France (IUF), F-75005, Paris, France

*Corresponding authors. Email: m.abdinejad@tudelft.nl, ali.seifitokaldani@mcgill.ca, and T.E.Burdyny@tudelft.nl

This PDF file includes:

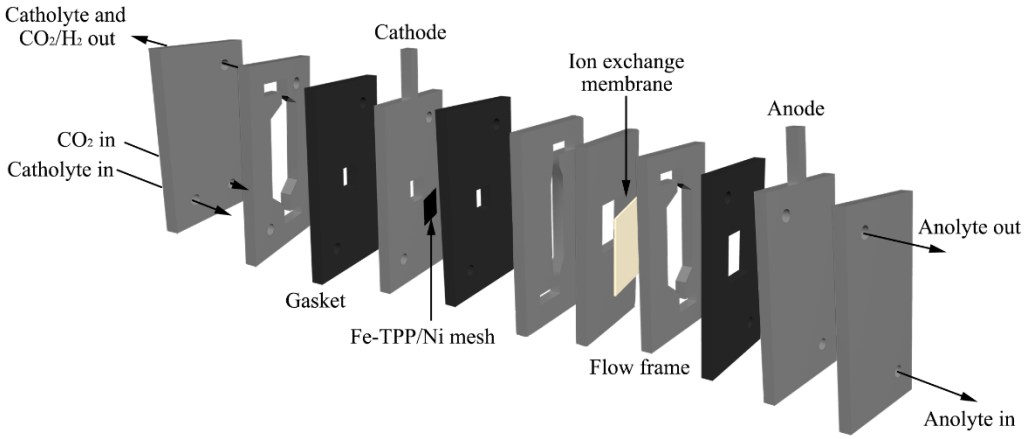

Fig. S1. Schematic illustration of the flow cell used for CO_2 electroreduction testing.

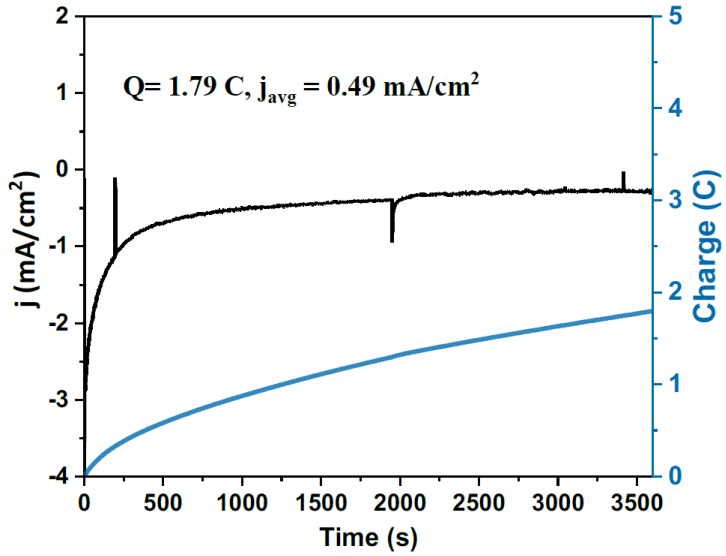

Fig. S2. CPE of a FeTPP/Ni foam (E = -0.30 V vs. RHE, t = 1 h) in CO-saturated 0.5 M $KHCO_3$ solution.

Table S1 – Linear combination fitting values in the range of -20 to +50 eV vs. the edge, where R-factor is equal to $\frac{\sum(fitted\ values - data)^2}{\sum data^2}$.

Voltage (V vs. RHE)	Weight of Fe (II)	Weight of Fe (III)	R-factor
-0.3	0.260 (±0.018)	0.740 (±0.008)	0.00217
-0.4	0.209 (±0.018)	0.791 (±0.009)	0.00285
-0.5	0.278 (±0.018)	0.722 (±0.008)	0.00279
-0.6	0.208 (±0.018)	0.792 (±0.009)	0.00287

Table S2. Best fitting EXAFS data for Fe-TPP on Ni

Scattering path	CN	R (Å)	R_{DFT} (Å)	σ^2 (Å^2)	ΔE_0 (eV)	R-factor
Fe-N	4.0	1.981	1.980	0.00681	- 3.727	0.02656

CN is the coordination number; R is the interatomic distance (the bond length between central iron atom and surrounding nitrogen atoms); R_{DFT} is the interatomic distance from DFT calculations; σ^2 is Debye-Waller factor (a measure of thermal and static disorder in absorber-scatterer distances); ΔE_0 is shift in edge-energy (the difference between the zero kinetic energy value and that of the theoretical model).

3D Electrode Manufacturing

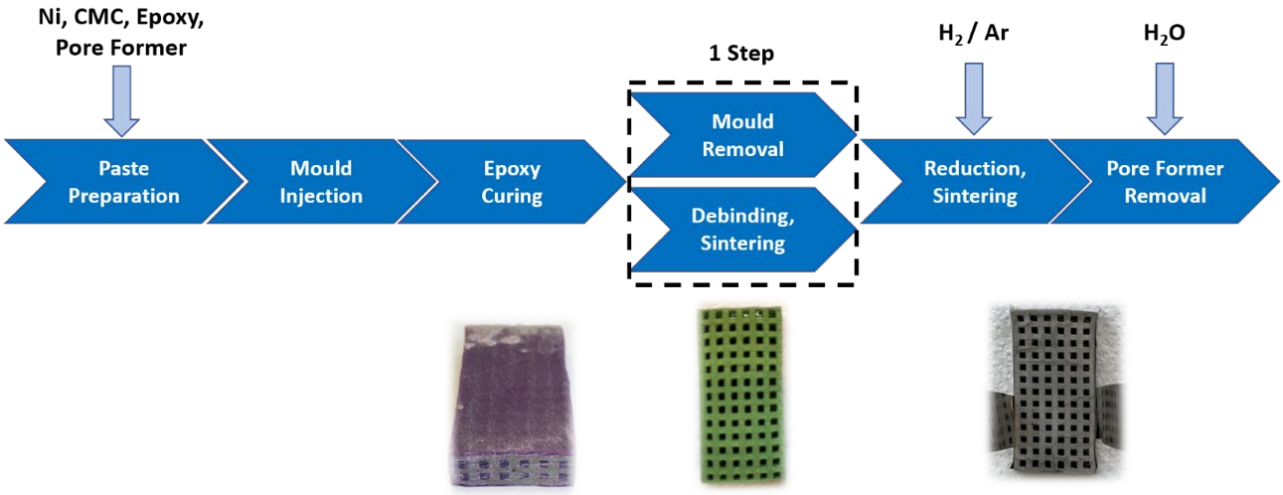

Fig. S3. Schematic of the 3D nickel electrode fabrication

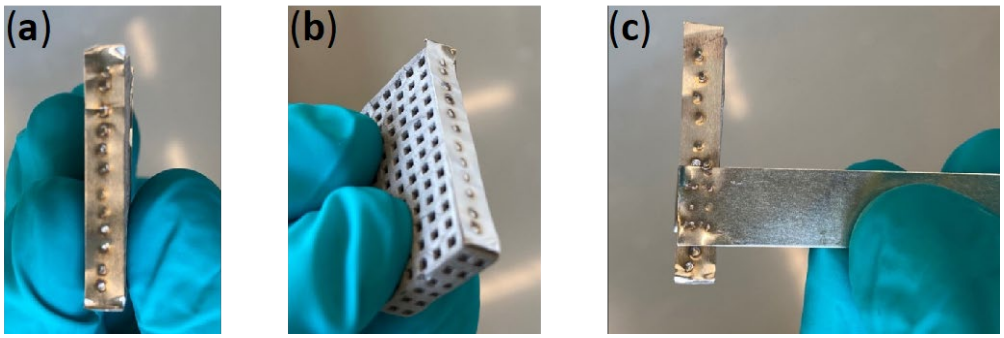

Fig. S4. Spot welding of nickel tabs onto the sintered 3D nickel electrode. (a and b) The nickel tab is first welded directly onto the side of the electrode. (c) Attaching the contact to the electrode.

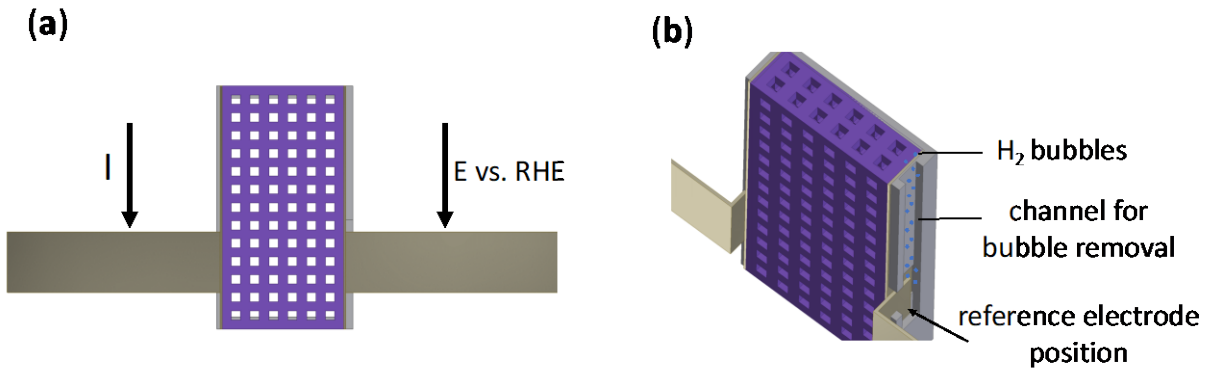

Fig. S5. (a) two-point electrode connection allowing for measurements excluding contact resistances. (b) Reduction of noise in the reference electrode channel by incorporating a bubble release channel in the electrode frame.

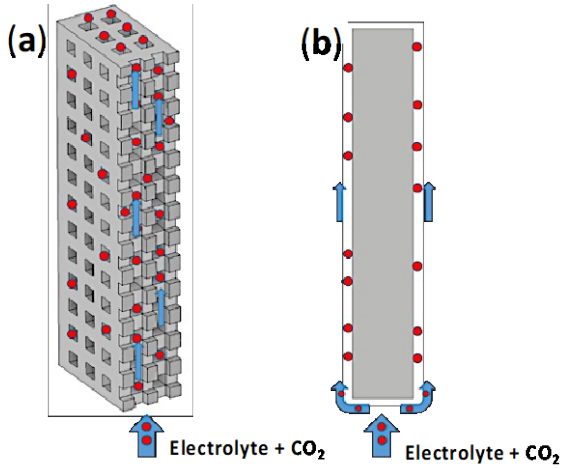

Fig. S6. Comparison of the mixed phase electrolyte and CO_2 flow between (a) 3D electrode and (b) conventional electrode.

Fig. S6 Text detail: An advantage of the presented 3D electrode is the improvement in electrode surface area that is in direct contact with the mixed phase flow consisting of the electrolyte and CO_2 bubbles (Fig. S6). As a result, CO_2-saturated electrolyte can flow through rather than past the electrode, leading to greater electrochemical surface area for the same planar surface area. To determine the increase in surface area of the 3D electrode compared to a non-3D electrode, we first measured the electrode dimensions of the sintered electrode and adjusted the original CAD model in Autodesk Inventor accordingly (Fig. S7). In the process of the mould removal, debinding, and sintering the electrode shrinks by 20 % in width and height, and 15 % in thickness. With the adjusted model the electrode surface area of all faces and the channels excluding microroughness is 40.49 cm^2. The volume excluding the channels is 1.69 cm^3.

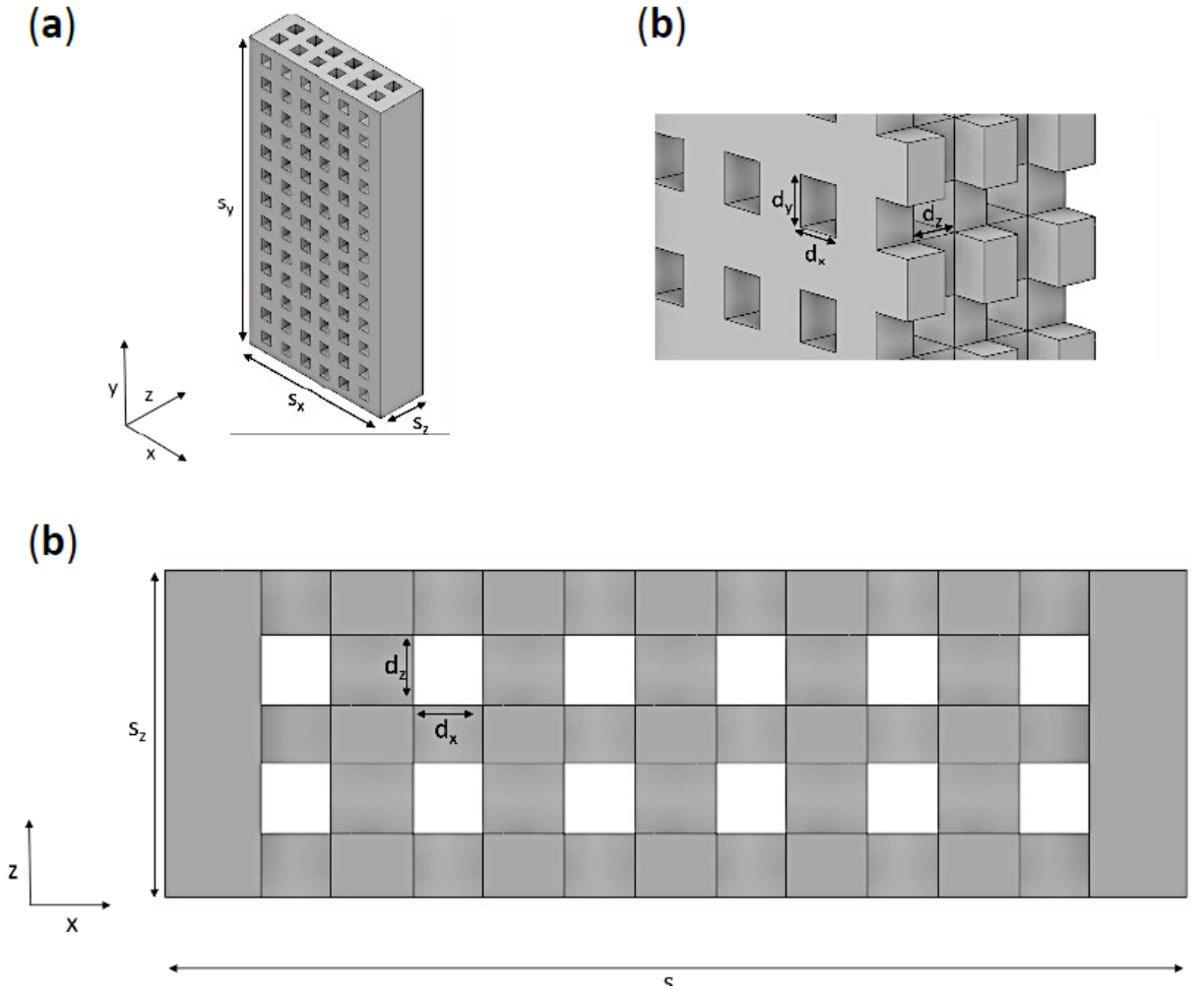

Fig. S7. Isometric view of the 3D electrode (a) and cut view of the 3D electrode showing the internal channel geometry (b, c). s_x = 16 mm, s_y = 32.3 mm, s_z = 5.1 mm, $d_x = d_y = d_z$ = 1.1 mm.

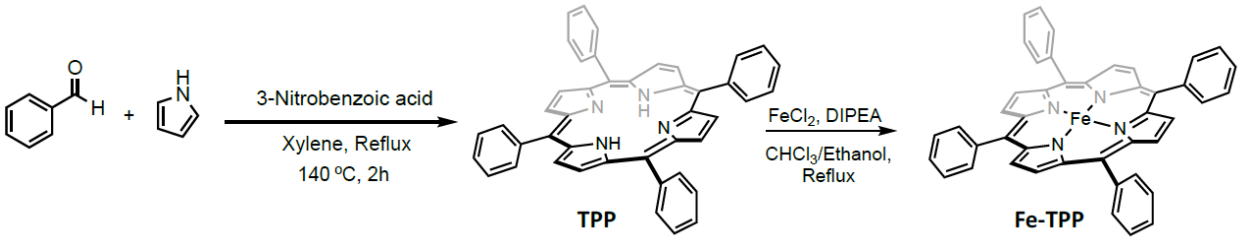

Scheme 1. Synthesis of tetraphenylporphyrin (TPP) followed by metallation reaction to form iron-tetraphenylporphyrin (Fe-TPP).

3D Electrode Characterization (Ni and Fe-TPP/Ni)

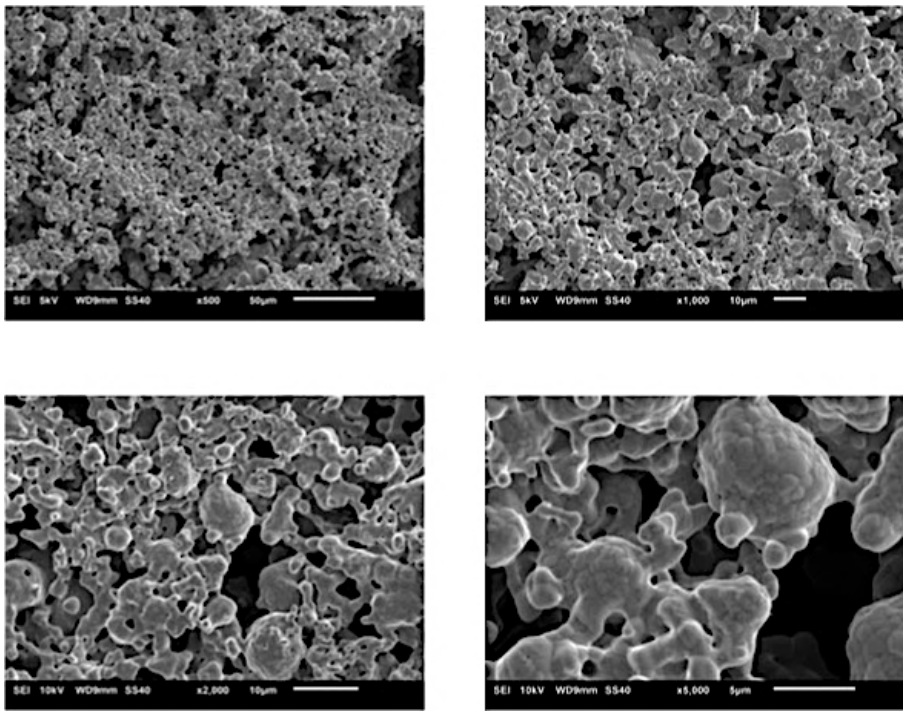

Fig. S8. Scanning electron microscopy (SEM) of the bare nickel electrode

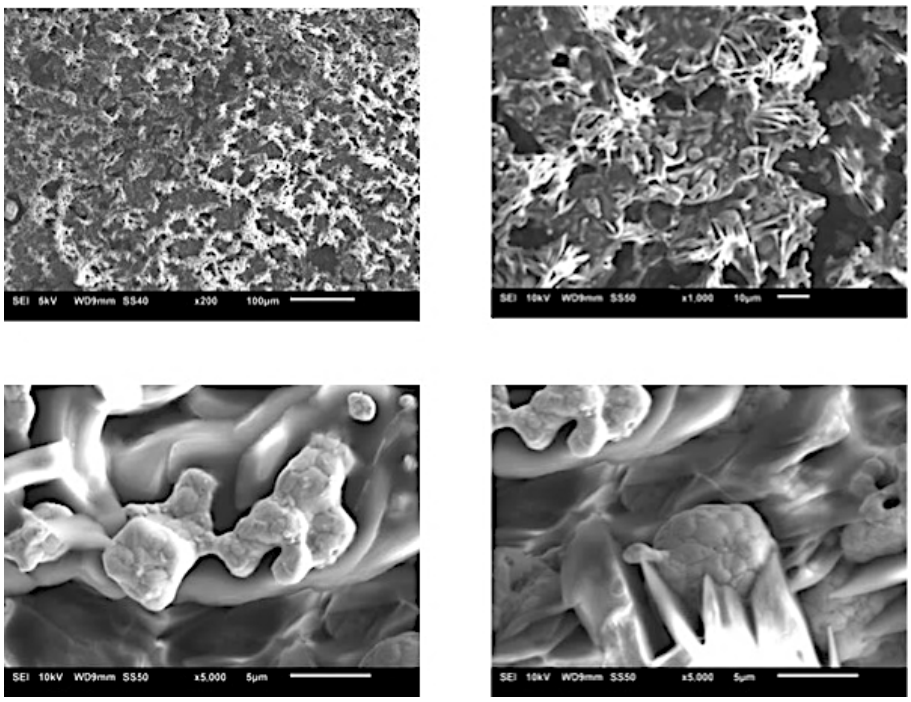

Fig. S9. Scanning electron microscopy (SEM) of the deposited Fe-TPP onto nickel electrode (Fe-TPP/Ni)

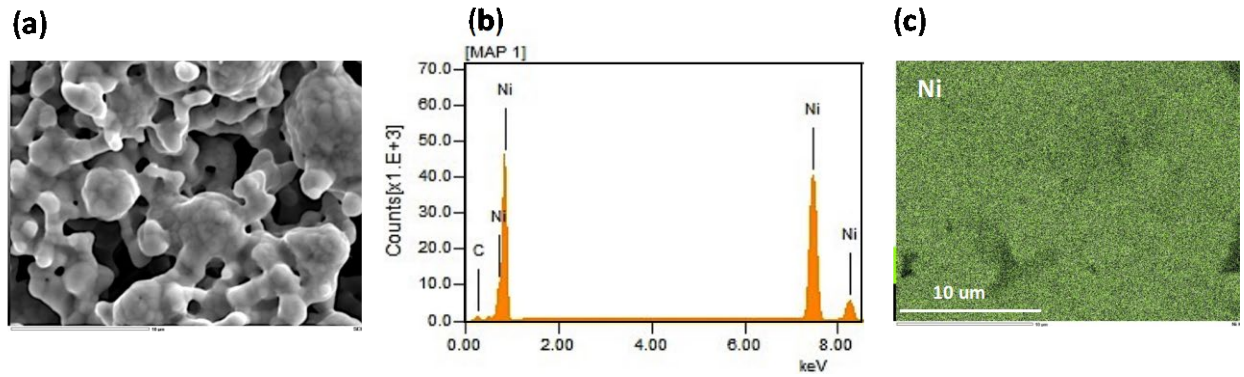

Fig. S10. (a) Scanning Electron Microscopy (SEM) of bare nickel electrode. (b) SEM mapping of elemental distribution. (c) Energy Dispersive X-rays Spectroscopy (EDX) of nickel.

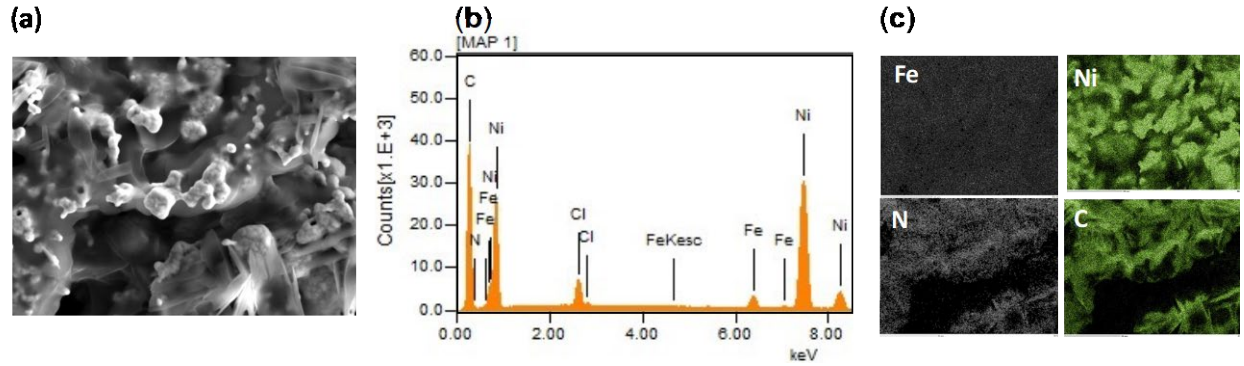

Fig. S11. (a) Scanning Electron Microscopy (SEM) of Fe-TPP/Ni electrode. (b) SEM mapping of elemental distribution. (c) Energy Dispersive X-rays Spectroscopy (EDX) of Fe, Ni, N, and C.

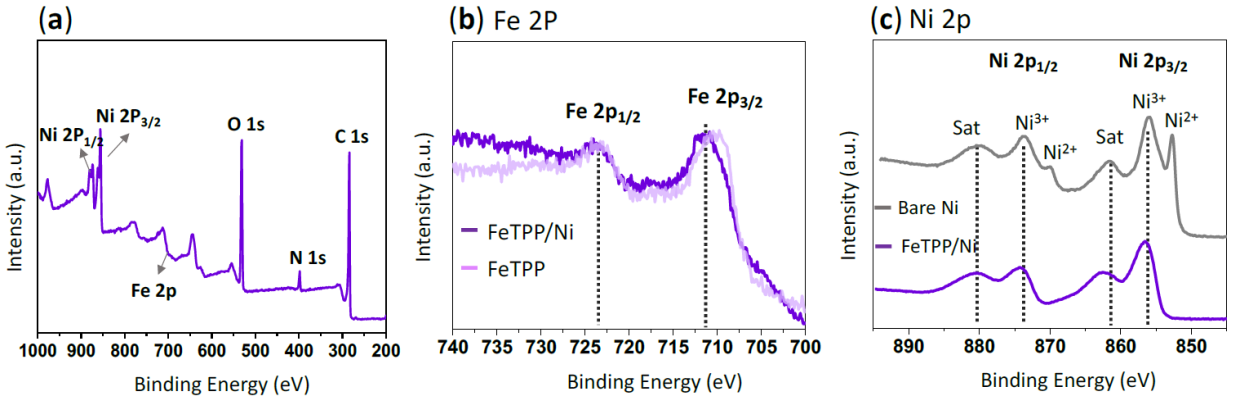

Fig. S12. (a) X-ray photoelectron spectra (XPS) survey of Fe-TPP/Ni electrode. The XPS of (b) Fe 2p; and (c) Ni 2p before and after deposition of Fe-TPP onto nickel electrode.

Figure S12 Additional text: The XPS survey shown in Fig. S12a indicates the characteristic peaks of Ni, Fe, N, C and O elements in Fe-TPP/Ni. The Fe 2p core-level XPS spectra before and after deposition onto nickel electrode show two characteristic peaks belonging to Fe $2p_{1/2}$ at 723.7 eV

and Fe $2p_{3/2}$ at 710.4 eV with a slight shift to the higher binding energy after deposition of Fe-TPP onto nickel electrode (Fig. S12b). These results are in agreement with previous reports.[1,2] The Ni 2p XPS spectra shown in Fig. S12c display two spin-orbital doublets located at 853.2 (Ni $2p_{3/2}$), 871.0 (Ni $2p_{1/2}$) corresponding to characteristics of Ni^{2+} revealing the coexistence of Ni or Ni $(OH)_2$.[3] The peaks at 856.1 (Ni $2p_{3/2}$), and 874.3 eV (Ni $2p_{1/2}$) can be assigned to the Ni^{3+} $2p_{3/2}$ and $2p_{1/2}$ orbitals, respectively. The co-existence of Ni^{2+} and Ni^{3+} is usually detected when fabricating nickel oxides on a nickel metal surface.[4,5] Just a small change in the binding energy of nickel is observed before and after the Fe-TPP deposition. The Ni^{2+} peak disappears in the case of Fe-TPP/Ni, which could be due to the interaction of the iron center of Fe-TPP with nickel. In Fig. S12c, XPS shows a slight shift of Ni 2p to higher binding energy could be either due to capturing CO_2 with the Fe center or the production of more oxidized Ni after the CO_2RR process in the aqueous environment. The characteristic N 1s peak 400.1 and 398.2 eV, assigned to pyrrolic and pyrrolic nitrogen, respectively. Deposition of Fe-TPP onto Ni formed a single peak at 398.45 eV attributed to N of Fe-N in Fe-TPP/Ni.[6,7]

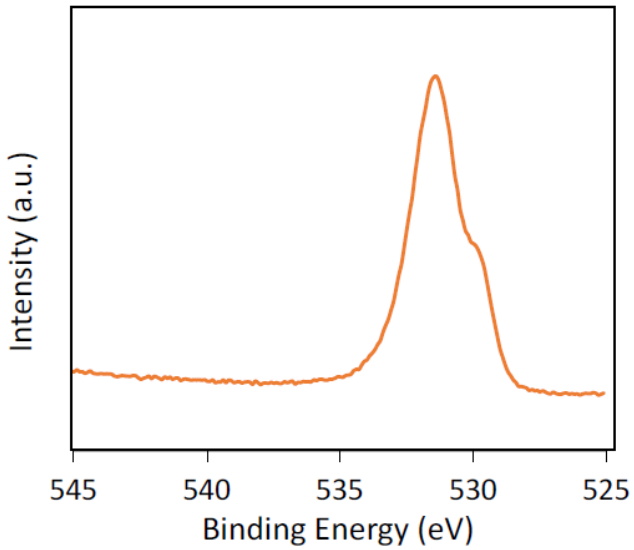

Fig. S13. X-ray photoelectron spectroscopy (XPS) characterization of O 1s for bare nickel electrode.

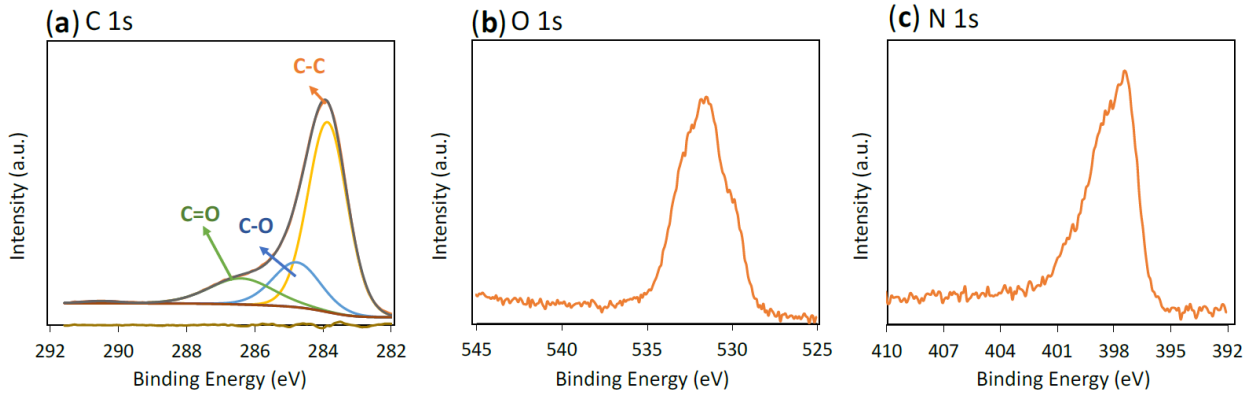

Fig. S14. X-ray photoelectron spectroscopy (XPS) characterization of the Fe-TPP/Ni electrode including (a) C 1s; (b) O 1s; and (c) N 1s spectra.

Experimental Set-Up

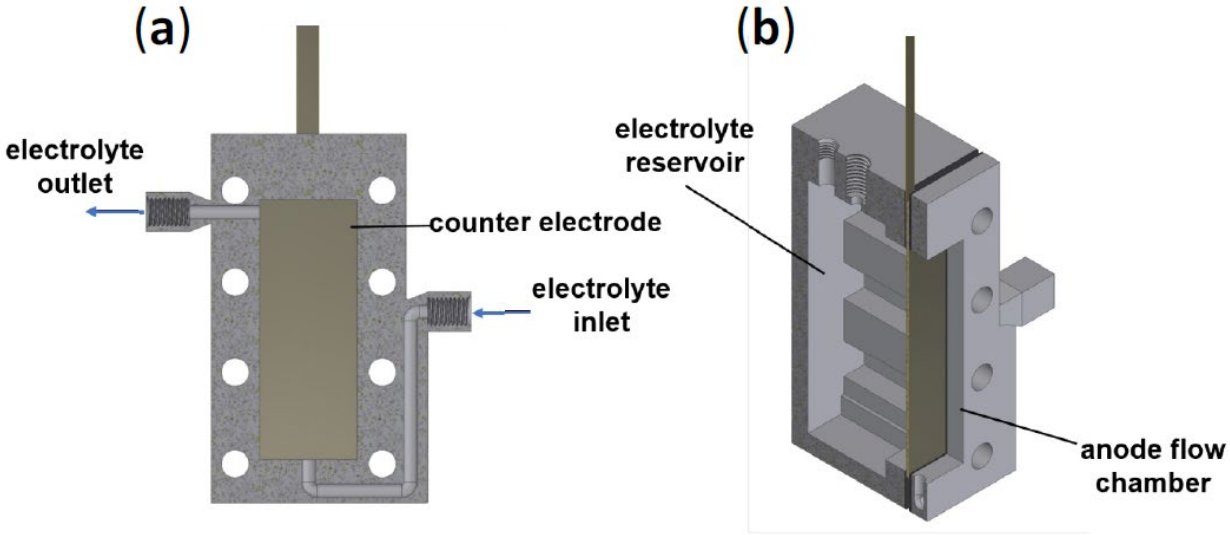

Fig. **S15.** Front (a) and isometric view (b) of the 3d-printed anode electrolyte reservoir and anode flow chamber.

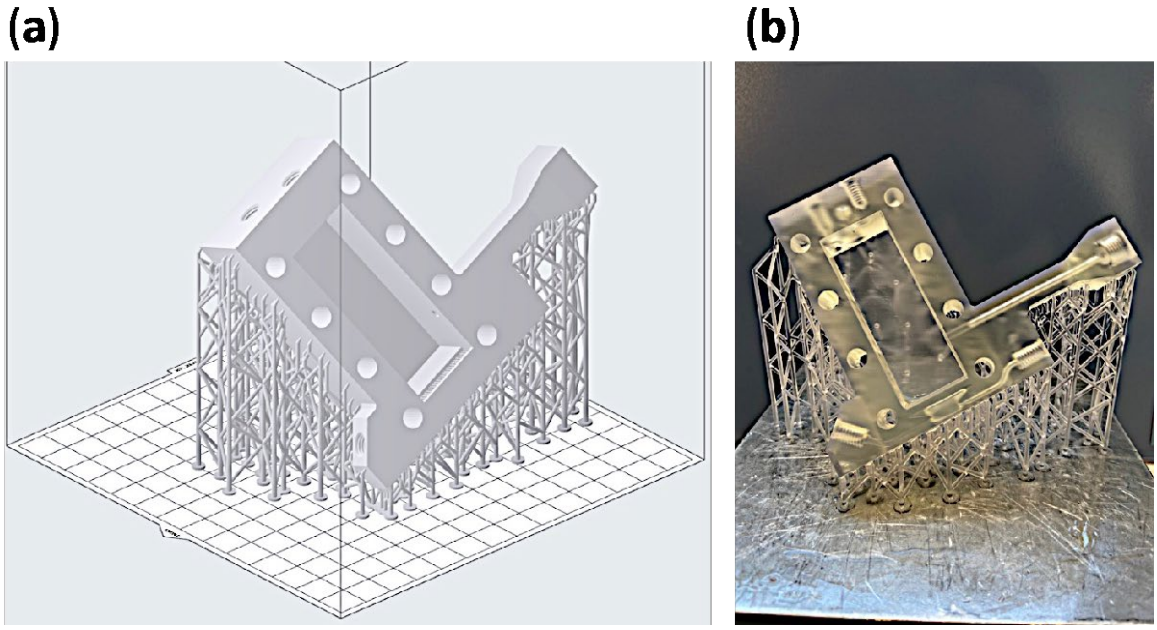

Fig. S16. 3D-printing of the CO_2RR Electrolyzer working electrode compartment. The cell is 3D-printed in clear resin on a SLA Formlabs Form 2 3D-printer. (a) Set-up of supporting structure prior 3D-printing. (b) Completed 3D-print before support structure removal, washing and curing.

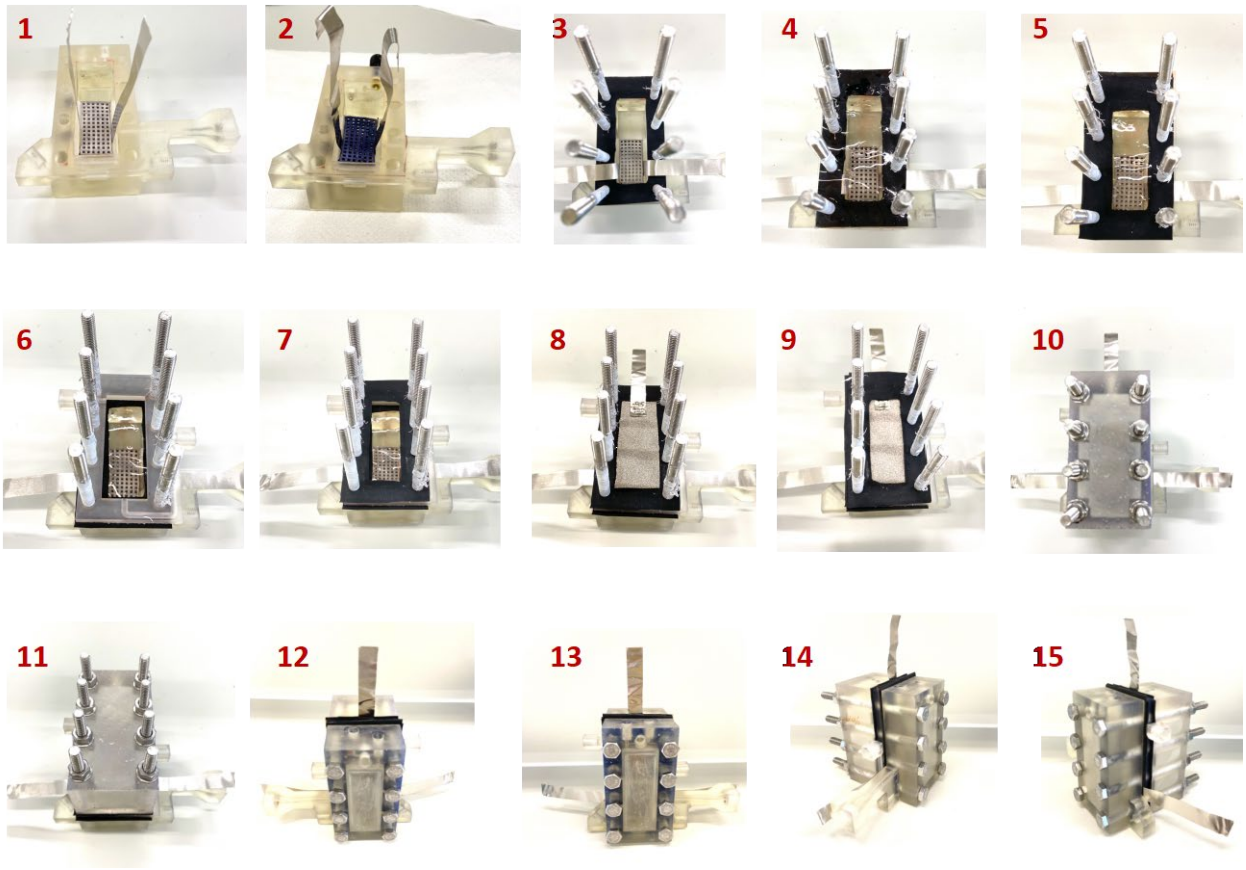

Fig. S17. Schematic of assembling the customized H-cell electrolyzer

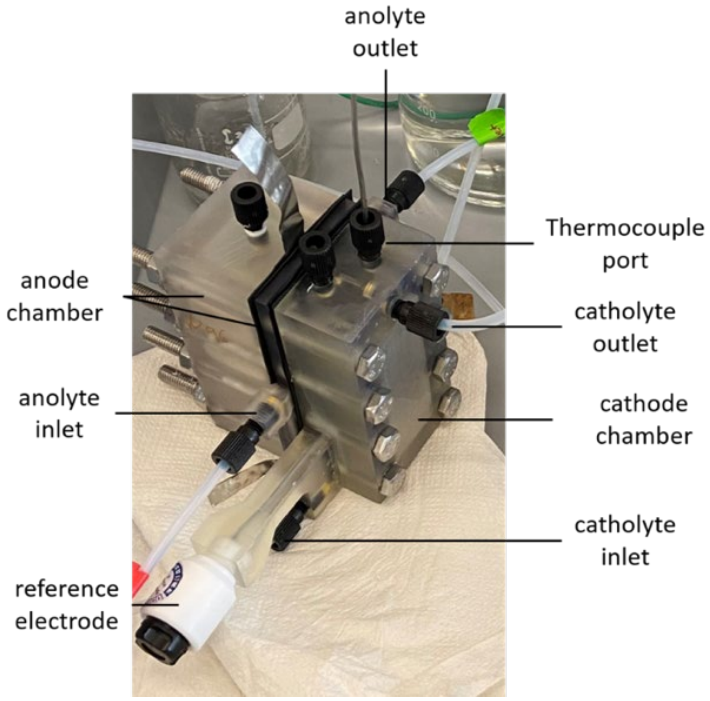

Fig. S18. Assembled CO_2-electrolyzer

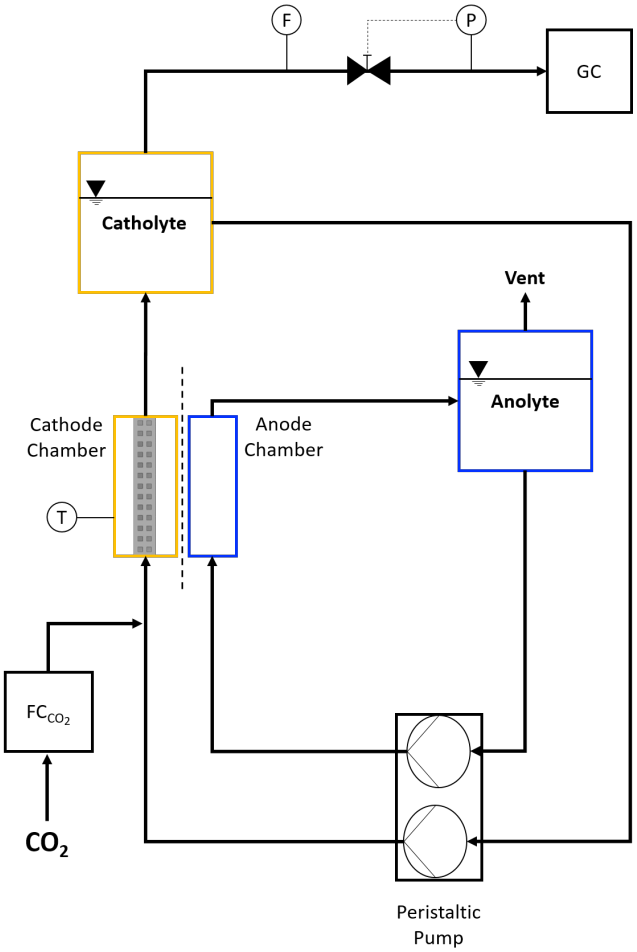

Fig. S19. Experimental set-up including the CO_2 flow controller (FC_{CO2}), the flow meter at the reactor outlet (F), the temperature measurement in the cathode chamber (T) and the gas chromatograph (GC). The pressure of the cathode circuit is controlled via a pressure control (P) in front of the GC.

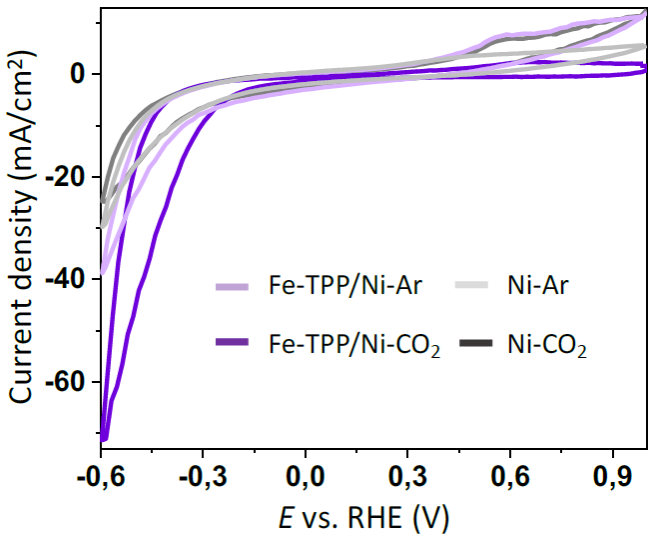

Fig. S20. Cyclic voltammetry (CV) comparison of bare nickel and Fe-TPP/Ni electrocatalysts under CO_2 and Ar with a scan rate of 100 mV/s in 0.5 M $KHCO_3$ with a flow electrolyte.

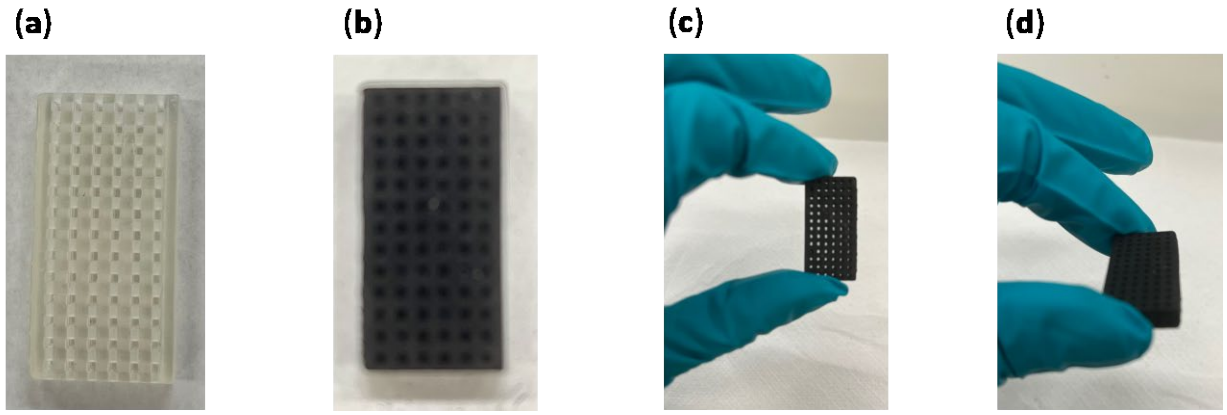

Fig. S21. Fabrication of the carbon black electrode by coating a 3D-printed template with carbon black. (a) Before coating, and (b) After coating (b-d).

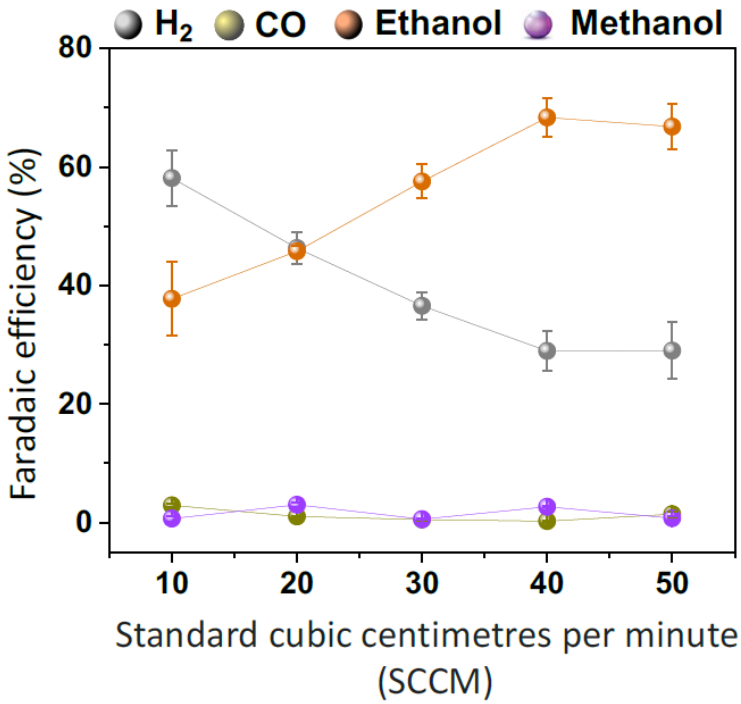

Fig. S22. CO_2 utilization and consumption for the flow rates of 10-50 SCCM using Fe-TPP/Ni at -0.3 V vs. RHE.

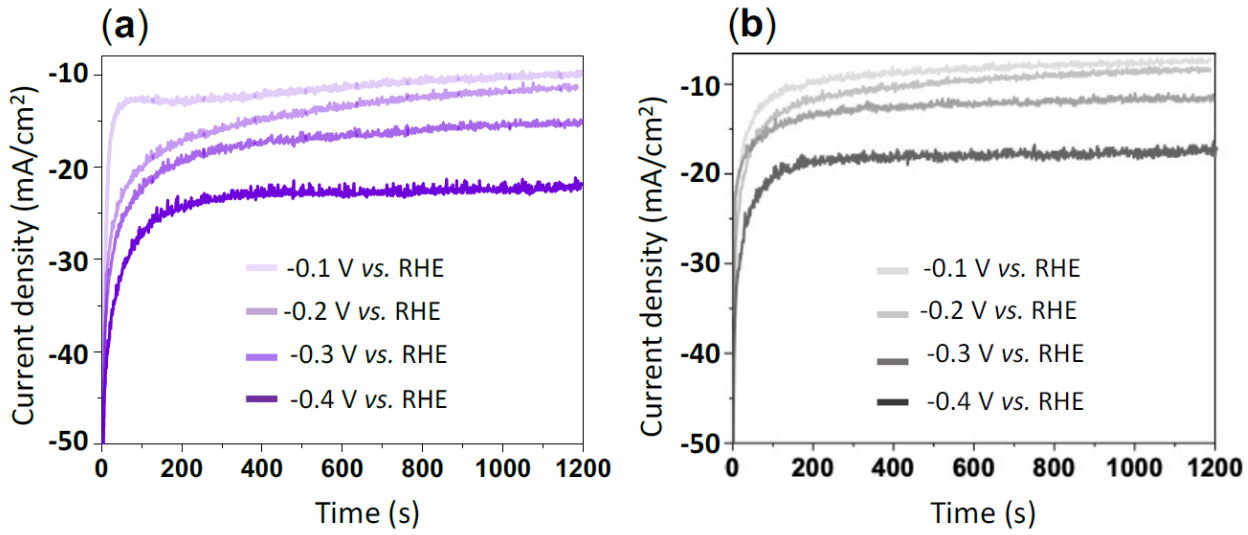

Fig. S23. Chronoamperometry of (a) Fe-TPP/Ni; and (b) bare nickel at -0.1, -0.2, -0.3, and -0.4 V vs. RHE with no flow.

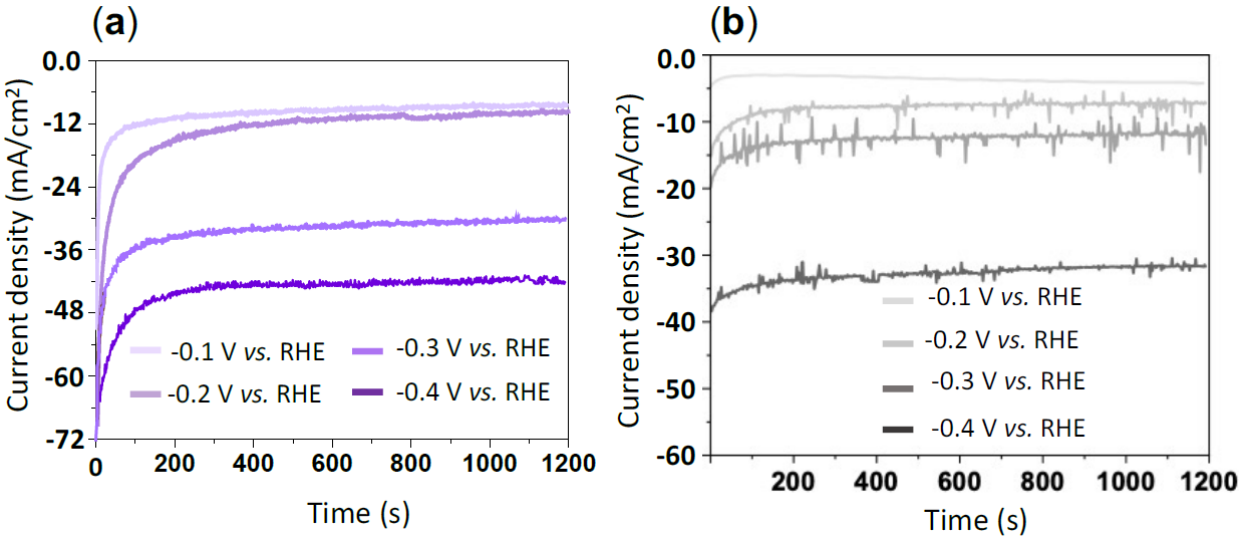

Fig. S24. Chronoamperometry of (a) Fe-TPP/Ni; and (b) bare nickel at -0.1, -0.2, -0.3, and -0.4 V vs. RHE with flow electrolyte.

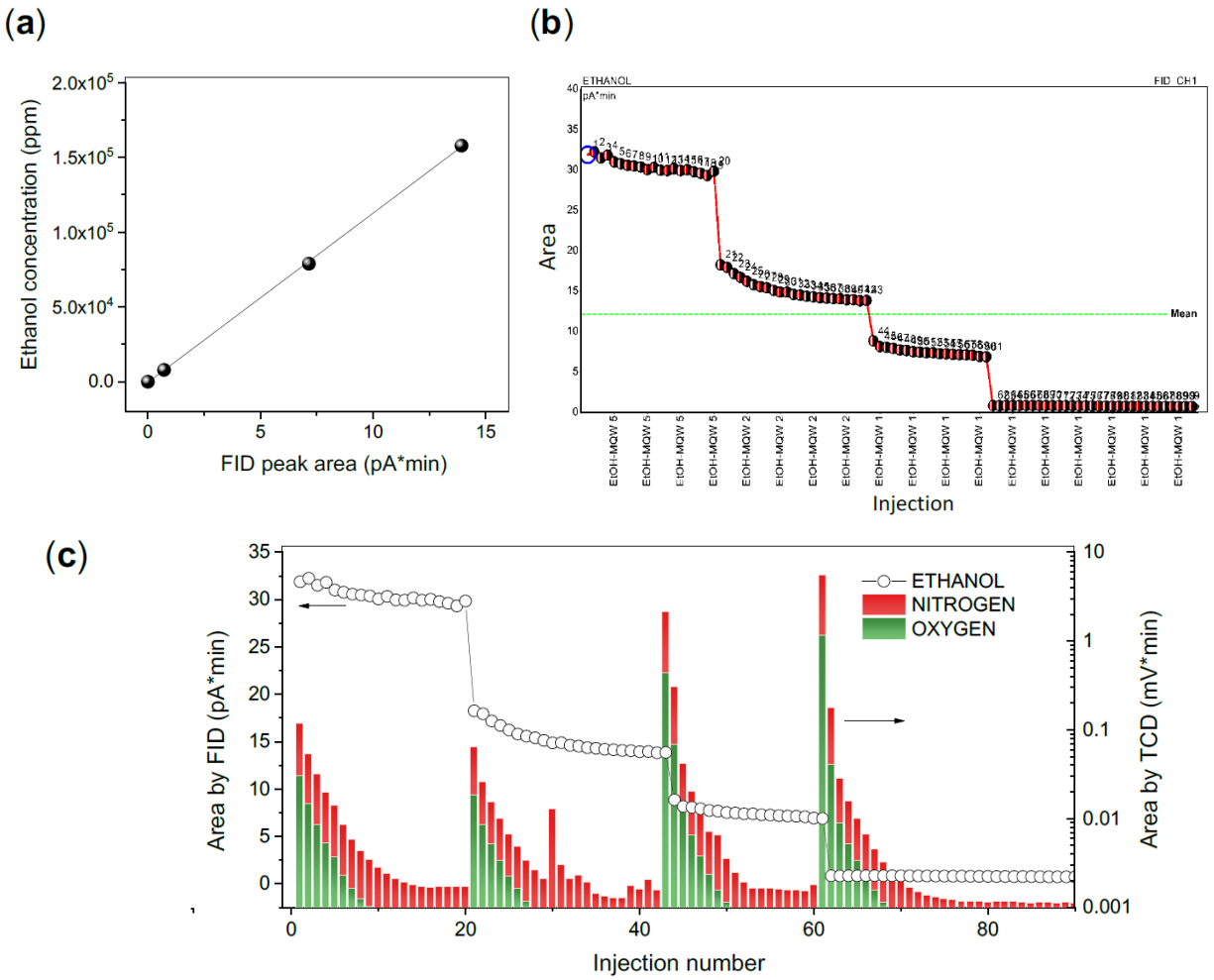

Fig. S25. (a) Calibration plots of Ethanol (in ppm) pervaporate vs. FID peak area; (b) Ethanol peak areas of the 92 GC injections as displayed by the GC-software Chromeleon®; and (c) Change of N_2 & O_2 concentration during the ethanol calibration, where the beaker was exposed to air while changing the concentration levels of the alcohol mixture.

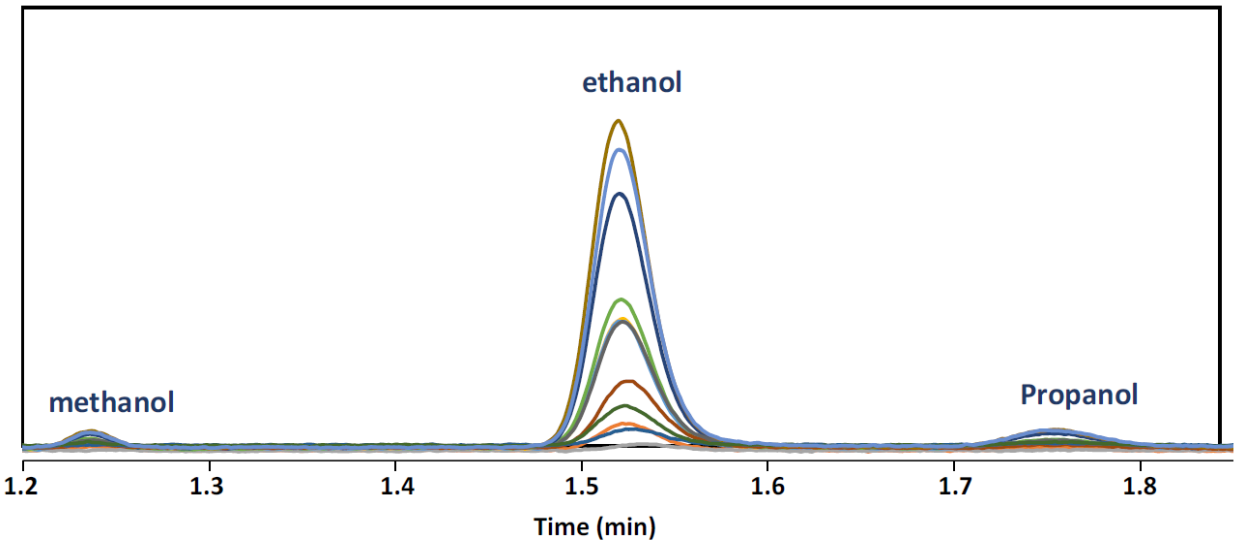

Fig. S26. Detected CO_2RR products using Gas Chromatography (GC) instrument.

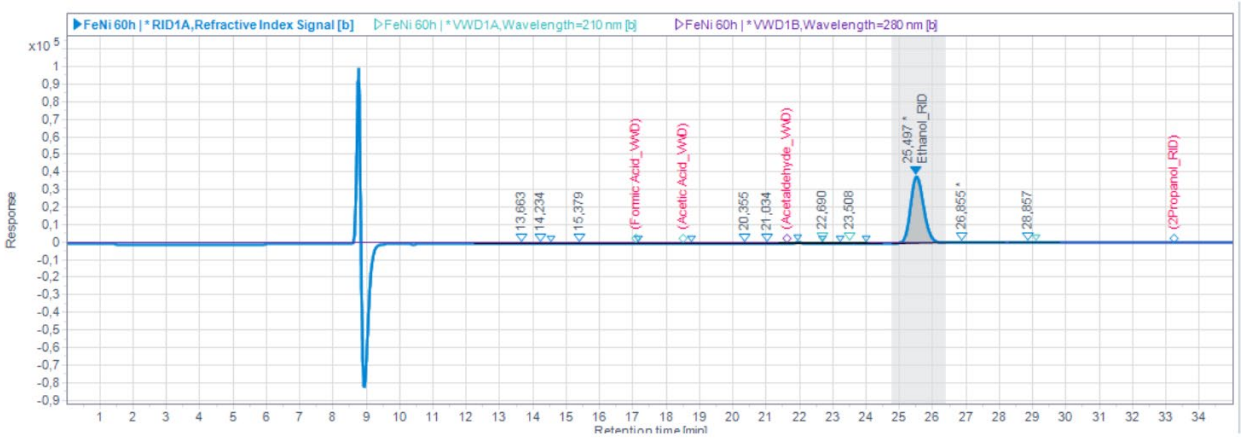

Fig. S27. Detected CO_2RR products using High-Performance Liquid Chromatograph (HPLC)

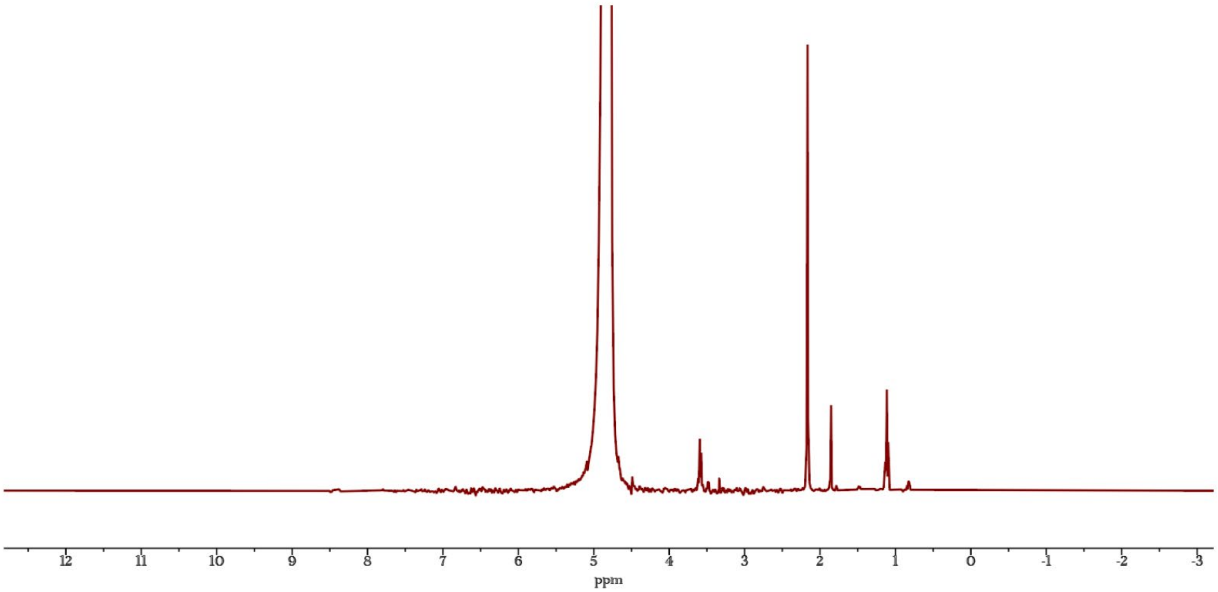

Fig. S28. An example of the proton Nuclear Magnetic Resonance (^{1}H NMR) spectrum of liquid products including ethanol at 1.17 and 3.64 ppm; trace amounts of methanol at 3.34 ppm, and propanol at 0.89, 1.54, and 3.56 ppm.

No reduced product was detected at -0.1 V vs RHE for either of the catalysts (Fig. S29). The formation of CO followed by ethanol as the major liquid product from Fe-TPP/Ni was first reliably identified at -0.2 V vs RHE with an FE of 37%. The selectivity of ethanol was increased to 68% at a more negative overpotential of -0.3 V vs RHE, which could be attributed to the increased electrochemical driving force.[9] At more negative potentials (-0.4 V vs RHE), the FE dropped to 32%, and an increase in HERs was observed.

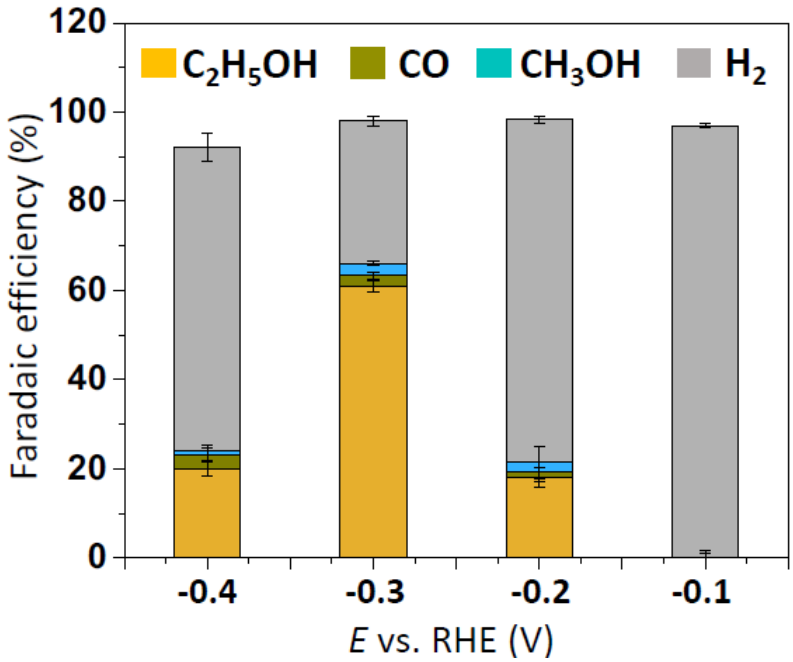

Fig. S29. Faradic efficiency (FE) of Fe-TPP/Ni after CO_2 electrolysis at -0.1, -0.2, -0.3, -0.4 V vs. RHE in 0.5 M $KHCO_3$ with no flow.

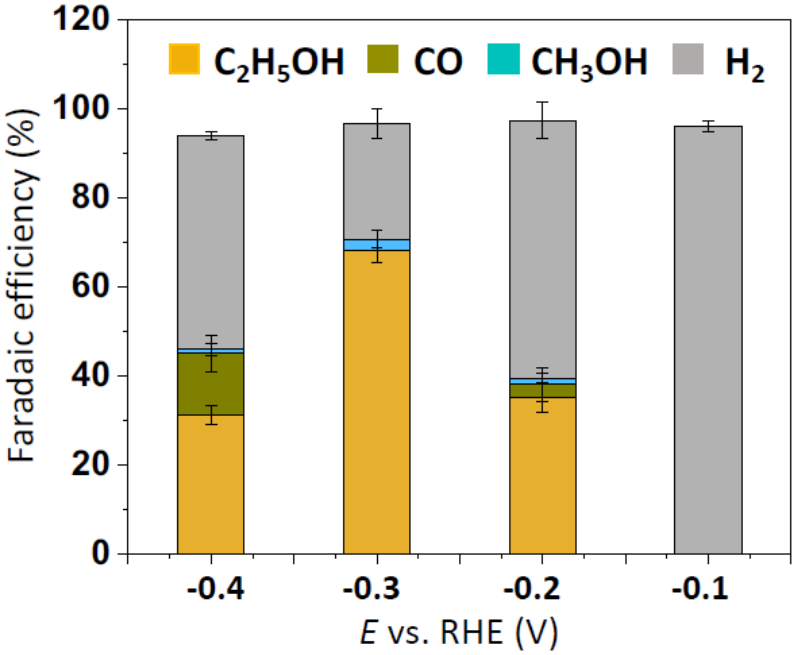

Fig. S30. Faradic efficiency (FE) of Fe-TPP/Ni after CO_2 electrolysis at -0.1, -0.2, -0.3, -0.4 V vs. RHE in 0.5 M $KHCO_3$ with flow.

Table S3 Additional text: To confirm the key role of the Fe-centered for product selectivity, control experiments on both metal-free porphyrin (TPP), and bare Ni, individually, were performed. As shown in Table S3, no liquid products were found, neither with bare nickel nor Fe-TPP/C. We

found that Fe-TPP/C complex undertook an electrocatalytic CO_2 reduction pathway only towards CO and H_2, i.e. very different from their iron analogues, illustrating the necessity of both Fe-TPP and 3D nickel electrode for the formation of ethanol.

Table S3. Product analysis of the heterogeneous bare nickel, Fe-TPP/Ni, and Fe-TPP/C catalysts in H-cell under flow. The reported data are the average values of three separate measurements taken from four individual reaction runs at various potentials.

Compound	Electrolyte	V vs. RHE	j (mA/cm^2)	FE% (Ethanol)	FE% (Methanol)	FE% (CO)	FE% (H_2)	Ref.
Ni	$KHCO_3$ (0.5 M)	-0.1	-0.35	0	0	0	98.7±1.5	Current work
	$KHCO_3$ (0.5 M)	-0.2	-0.8	0	0	0	99.3±1.3	Current work
	$KHCO_3$ (0.5 M)	-0.3	-14	0	0	8±0.5	91 ±2	Current work
	$KHCO_3$ (0.5 M)	-0.4	-32	0	0	14±2	85±2.4	Current work
Fe-TPP/Ni	$KHCO_3$ (0.5 M)	-0.1	-8	0	0	0	95±3.2	Current work
	$KHCO_3$ (0.5 M)	-0.2	-11	37±5.5	1.3±0.2	3±0.2	58±5.3	Current work
	$KHCO_3$ (0.5 M)	-0.3	-31	68±3.2	2.7±0.2	0	26±3.4	Current work
	$KHCO_3$ (0.5 M)	-0.4	-42	32±1	0.1±0.3	11±1	52±1.7	Current work
Fe-TPP/C	$KHCO_3$ (0.5 M)	-0.5	-6.7	-	-	28±3.1	67±4.7	Current work
	$KHCO_3$ (0.5 M)	-0.6	-7.4	-	-	52±3.2	48±1.6	Current work
	$KHCO_3$ (0.5 M)	-0.7	-7.9	-	-	43±3.9	55±2.8	Current work
	$KHCO_3$ (0.5 M)	-0.8	-8.2	-	-	31±1.6	69±3.7	Current work

Figure 2a and 2b Additional Text: To understand the strength of the interaction between the Fe-TPP and the support, we looked into the adsorption energies calculated by DFT computations. The simulated supports need to be large enough, so the adsorbed Fe-TPP is not affected by the imaginary neighbours existing in the periodic boundary conditions applied in the DFT. Due to computational limitations, we had to modify the Fe-TPP molecule by substituting benzene cycles with a hydrogen atom (to reduce the size of the computations), as suggested in the literature.[14,15] We optimized the modified Fe-TPP on graphene structure and the nickel surface. Results showed a significant difference in the adsorption distances. While the distance between Fe atom and the nickel surface is 2.00 Å, revealing a strong adherence and chemisorption, it increases to 3.92 Å on graphene, revealing a weak physisorption (Fig. 2a and 2b). Charge delocalization plots (Fig. 2a and 2b), show qualitatively the stronger interaction between the Fe-TPP molecule and nickel surface compared to that with graphene. There is a larger electron donation to the chemical bond between Fe and Ni, while the electronic structure of carbon atoms on graphene looks intact. Bader charge analysis exhibited only 0.061 increase in the oxidation state of Fe atom when exposed to the carbon. However, the nickel surface donates more electrons and decreases the oxidation state of Fe by 0.222, enabling the active site to donate more electrons during the reduction reaction.

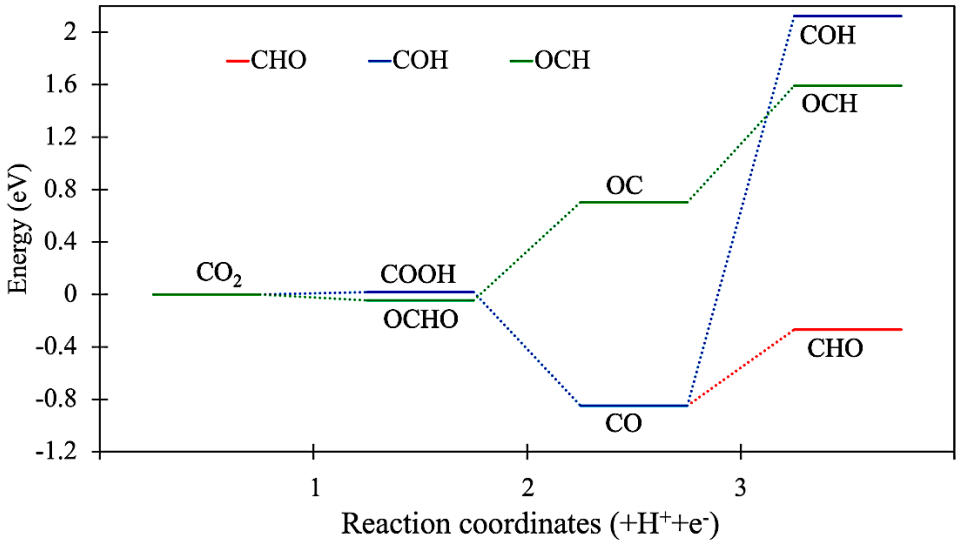

Fig. S31 – Energy diagram of the protonation of mono-carbon species

Table S4 Additional Text: The formation of C_{2+} products occur either through *CO dimerizes to form *OCCO at low overpotentials,[10] to be converted to *OCCOH[11] through a hydrogenation reaction, or via *CO hydrogenation to form *CHO,[12] which takes place at high overpotentials. It should be noted that the C–C coupling step is highly sensitive to the structure and morphology of the catalyst and should profit from high local density of C intermediates.[13] In the both the flow-cell and 3D electrode experiments a delay in ethanol formation was observed, potentially indicating a slow saturation of carbon intermediates.

Table S4 – C-C coupling barriers for different considered cases

Reaction	COH + COH	CHO + CHO	CO + CO	COH + CHO	COH + CO
Barrier (eV)	-2.77	0.297	2.04	-1.98	-0.646

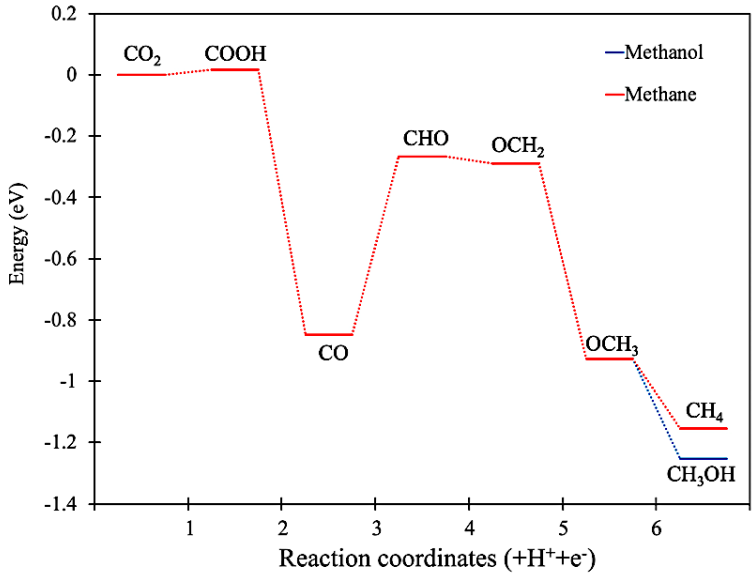

Fig. S32 – Energy diagram of further protonation of CHO towards methane and methanol formation targets

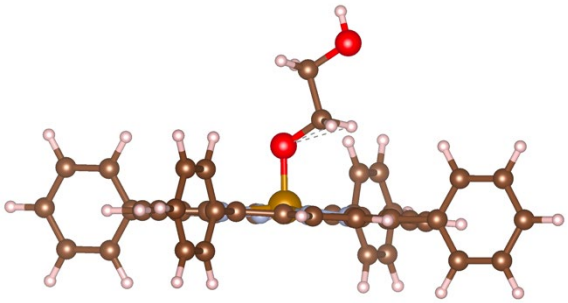

Fig. S33 – Key reaction intermediate (*OCH_2CH_2OH)

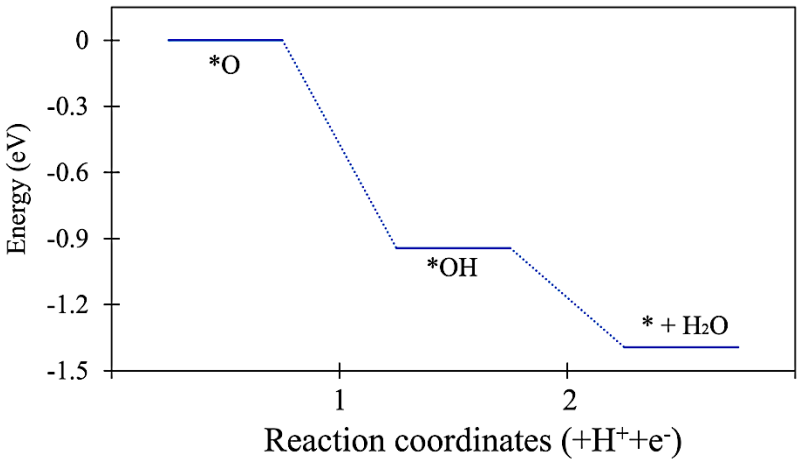

Fig. S34 – Oxygen removal from the surface and site recovery barrier, * stands for the catalytic site and *i corresponds to the adsorbed I species.

Table S5 Additional Text: Table S5 demonstrates the oxidation state of Fe atom with different adsorbates. The oxidation state of Fe slightly increases (i.e., it donates electrons) when CO_2 is close enough to the Fe-TPP and adsorbed on the surface. Following the first PCET step to produce *COOH, we observe that Fe oxidation state is 1.0289, which is 0.3863 higher compared to that before the PCET step. Assuming that the PCET step itself requires 1 electron coming from the Fe-TPP, in fact, Fe should provide 1.3863 electrons to form *COOH. Similar calculations are performed for the subsequent PCET steps, as shown in Table S5. Through these calculations, we observed two interesting phenomena: (*i*) *CO protonation to form *CHO decreases the total number of electrons that Fe has to donate to the adsorbate from 0.7041 to 0.2004 electrons, thereby stabilizing the *CHO on its surface, and (*ii*) *CHO protonation to $*OCH_2$ and subsequent steps to form methane requires a larger electron donation by Fe (0.6181 electrons) compared to the coupling step (0.3081 electrons), again stabilizing the *OCHCHO adsorbates more favorably than $*OCH_2$. Therefore, we posit that although both ethanol and methane pathways are downhill after the rate-determining step of *CHO formation, because of a more favorable electronic structure, the active site of Fe will be recovered easier through the ethanol pathway.

Table S5 – Results of Bader charge analysis on different reaction intermediates

Specie	Charge	Oxidation number	Number of e^- transferred (in step)	Expected difference in the oxidation number with respect to the donated e^-	Accumulated increase in oxidation numbers after donating e^-	Overall Number of e^- transferred	Difference between the accumulated increase in oxidation number and total number of donated electrons
Fe-TPP	7.5353	0.4647	0	-	0.4647	0	0.4647
Fe-TPP + physiosorbed CO_2	7.3574	0.6426	0	-	-	-	-
Fe-TPP-COOH	6.9711	1.0289	1	1.3863	1.3863	1	0.3863
Fe-TPP-CO	6.6533	1.3467	1	1.3178	2.7041	2	0.7041
FeTPP-CHO	7.157	0.843	1	0.4963	3.2004	3	0.2004
FeTPP-OCH_2	6.7393	1.2607	1	1.4177	4.6181	4	0.6181
FeTPP-OCH_3	6.7628	1.2372	1	0.9765	5.5946	5	0.5946
FeTPP-O	6.6449	1.3551	1	1.1179	6.7125	6	0.7125
FeTPP-OCHCHO	6.8489	1.1511	0	0.3081	-	-	-

Table S6 – Energy levels of studied species in this work (in eV)

Species	Energy (eV)	Species	Energy (eV)	Species	Energy (eV)
H_2O	-14.216	Fe-TPP-CHOCOH	-577.156	Fe-TPP-$OCHCH_2O$	-579.837
H_2	-6.734	Fe-TPP-CHOCHO	-577.065	Fe-TPP-OCHCHOH	-580.905
Fe-TPP	-539.315	Fe-TPP-COCOH	-573.033	Fe-TPP-OCH_2CHOH	-583.563
Fe-TPP-CO_2	-562.425	Fe-TPP-COHCO	-573.036	Fe-TPP-$OCHCH_2OH$	-584.706
Fe-TPP-COOH	-565.638	Fe-TPP-COCO	-569.958	Fe-TPP-OCH_2CH_2O	-583.505
Fe-TPP-CO	-555.655	Fe-TPP-OCHO	-565.700	Fe-TPP-OCH_2CH_2OH	-588.736
Fe-TPP-CHO	-558.442	Fe-TPP-OC	-554.103	Fe-TPP-OH	-549.714
Fe-TPP-CHOH	-561.704	Fe-TPP-OCH	-556.580	Fe-TPP-O	-545.403
Fe-TPP-COH	-556.050	Fe-TPP-OCH_2	-561.829	Fe-TPP-O + Ethanol	-592.290
Fe-TPP-C	-546.025	Fe-TPP-OCHCHO	-577.362	Fe-TPP-OCH_2 + Methanol	-591.875
Fe-TPP-COHCOH	-575.556	Fe-TPP-OCH_2CHO	-581.102	Fe-TPP-OCH_2CH_2	-576.820

Additional DFT Text: One of the crucial reaction steps is the C-C coupling. Toward producing ethanol, CHO should experience a coupling step rather than further protonation. Comparing these two different steps, fig. S35 shows that Fe atom in the center of Fe-TPP shows a higher activity level in charge delocalization. Therefore, more interaction is expected between the catalyst and coupled species. To provide a fair comparison, the charge delocalization graphs in Fig. S35 and S36 are plotted at the same isosurface levels.

As shown in Table S5, we ran Bader charge analysis on different reaction intermediates toward methane production and coupling step. We observe that in reductive potentials, the trend of the change in oxidation numbers from *CO (shown in blue) to *CHO (shown in green) is negative, while it becomes positive in the case of *CHO to *OCH_2 (shown in red). Therefore, we can suggest that in this reduction process, the surface consumes some electrons in the latter case to evolve, in competition with the electron demanding reaction. Now comparing this protonation step with the coupling step, we can also notice in the fifth column that the change from *CHO to *OCHCHO is negative and smaller than moving toward *OCH_2 (towards methane production).

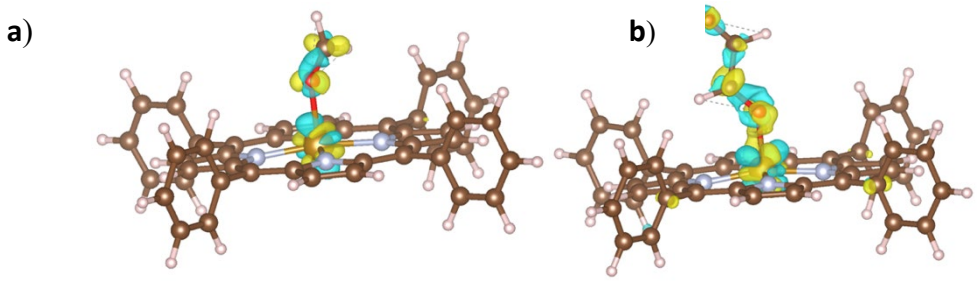

Fig. S35 – Charge delocalization of a) *OCH_2 and b) *OCHCHO, both with an isosurface level of 0.008 e.Bohr^{-3}.

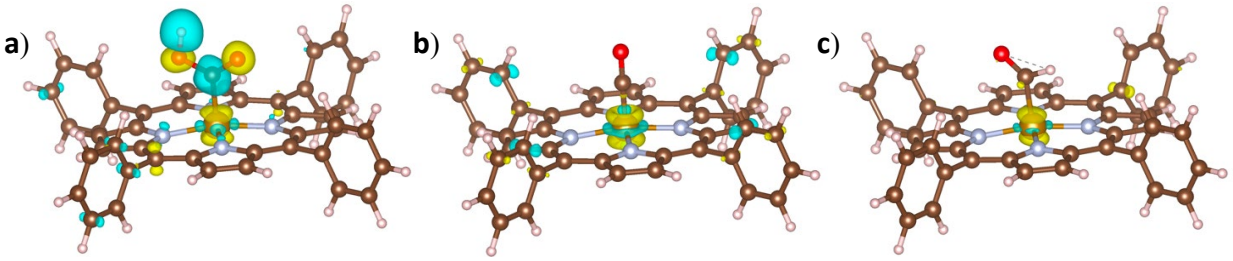

Fig. S36 – Charge delocalization of a) *COOH, b) *CO, and c) *CHO at isosurface level of 0.08 e.Bohr^{-3}.

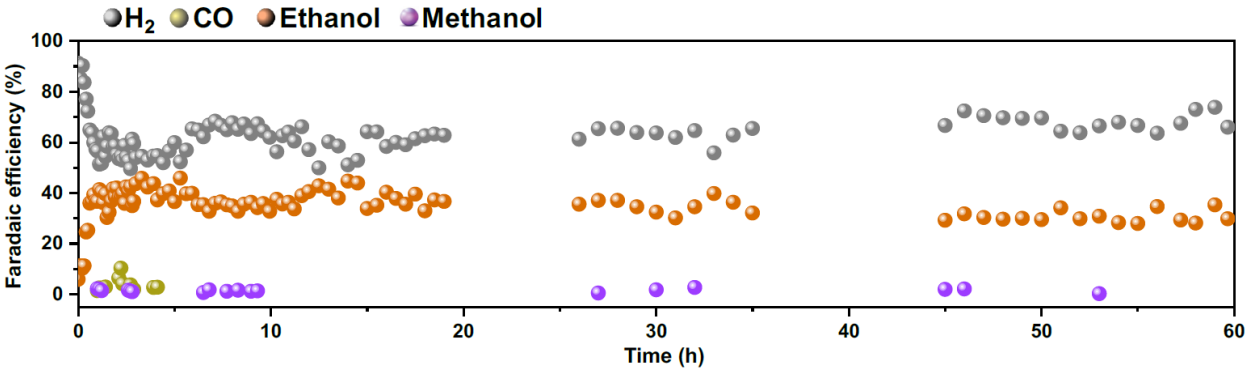

Fig. S37. Long-term stability test of FeTPP/Ni at a constant potential of -0.3 V vs RHE in 0.5 M $KHCO_3$ with 10 SCCM.

The loss of ~5% loss of the amount of porphyrin during the 60h reaction time, could be due to the aggregated porphyrins on the electrode surface, which can't stay for a long time during the reaction period, which might be the cause of the slight decrease of FE after a few hours during the CO_2RR.[16,17] Therefore, we hypothesized that the degradation is attributed to the mass loss of the Fe-TPP molecules on the Ni substrate. This observation was further confirmed using a Keyence VHX-7000 optical microscope (fig. S38 and S39),[18] which indicates some aggregation of the molecular porphyrin catalysts that occurred during the immobilization step.

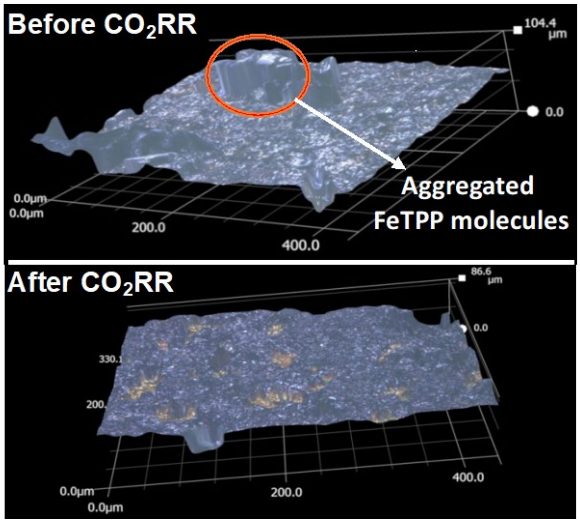

Fig. S38. 3D view of Fe-TPP/Ni electrode surface before and after 60h electrochemical CO_2RR taken using Keyence VHX7000 digital microscope and optical profiler.

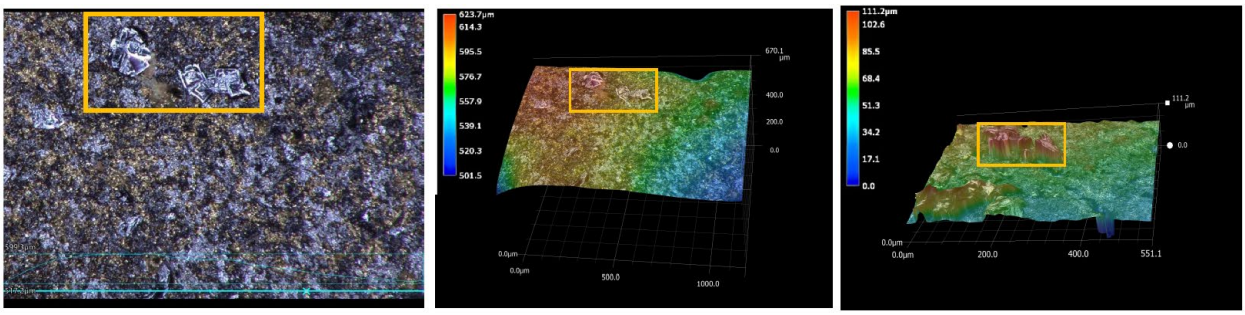

Fig. S39. Highlighted molecular aggregation on Fe-TPP/Ni electrodes. The images were taken with the Keyence VHX7000 digital microscope and optical profiler.

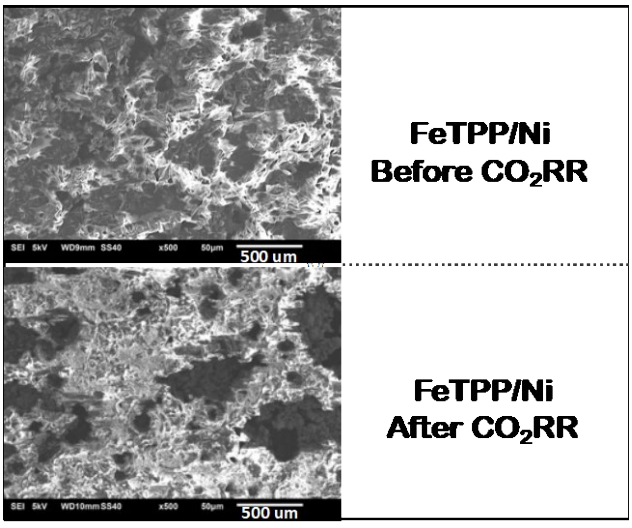

Fig. S40. Scanning Electron Microscopy (SEM) comparison before and after 62 hours of electrolysis.

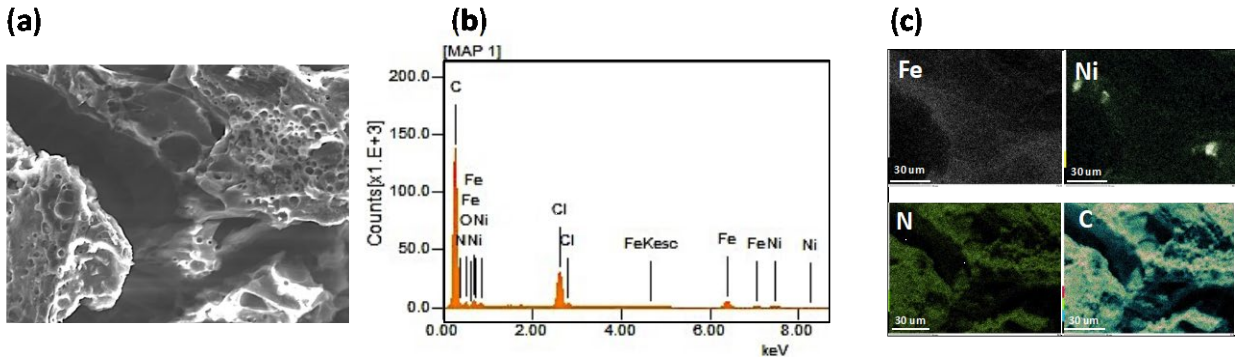

Fig. S41. (A) Scanning Electron Microscopy (SEM) of Fe-TPP/Ni electrode. (B) SEM mapping of elemental distribution. (C) Energy Dispersive X-rays Spectroscopy (EDX) of Fe, Ni, N, and C after 62 hours of electrolysis.

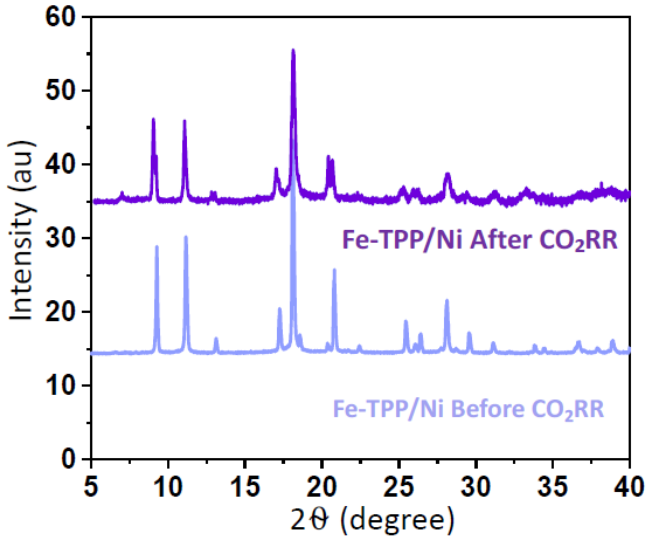

Fig. S42. X-ray Diffraction (XRD) comparison of Fe-TPP/Ni before and after 62 hours of electrolysis.

Figure S42 Additional Text: The deposited Fe-TPP catalytic layer was characterized by powder X-ray diffraction (XRD) (Fig. S42) and X-ray photoelectron spectroscopy (XPS) further confirmed that Fe-TPP was successfully immobilized onto nickel electrode surface. The XRD was performed using a Bruker D8 Advanced diffractometer with Cu-Kα source (Cu radiation wavelength: Kα1(100) = 1.54060 Å, Kα2(50) = 1.54439 Å) and Lynxeye-XE-T position sensitive detector. Using XRD, we confirmed no degradation or decomposition occurred after long-term electrolysis.

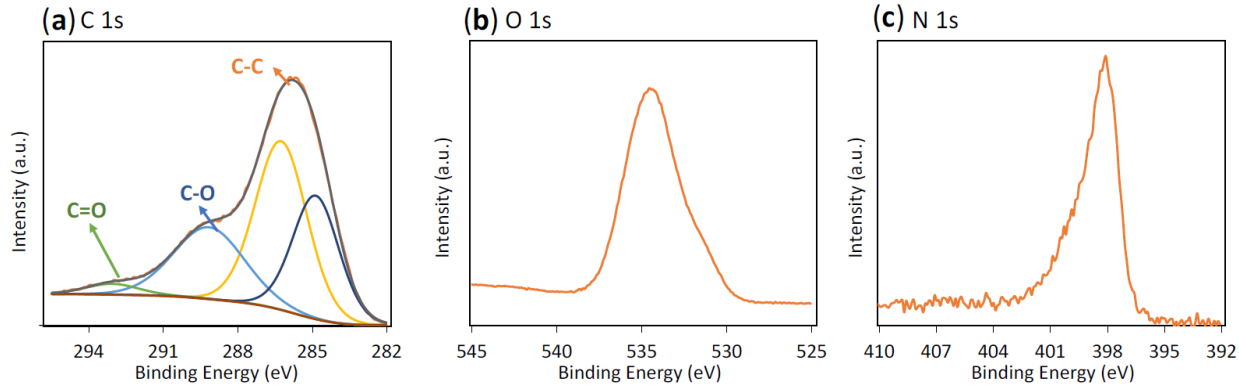

Fig. S43. X-ray photoelectron spectroscopy (XPS) characterization of the Fe-TPP/Ni electrode including (a) C 1s, (b) O 1s, and (C) N 1s spectra after electrochemical CO_2RR.

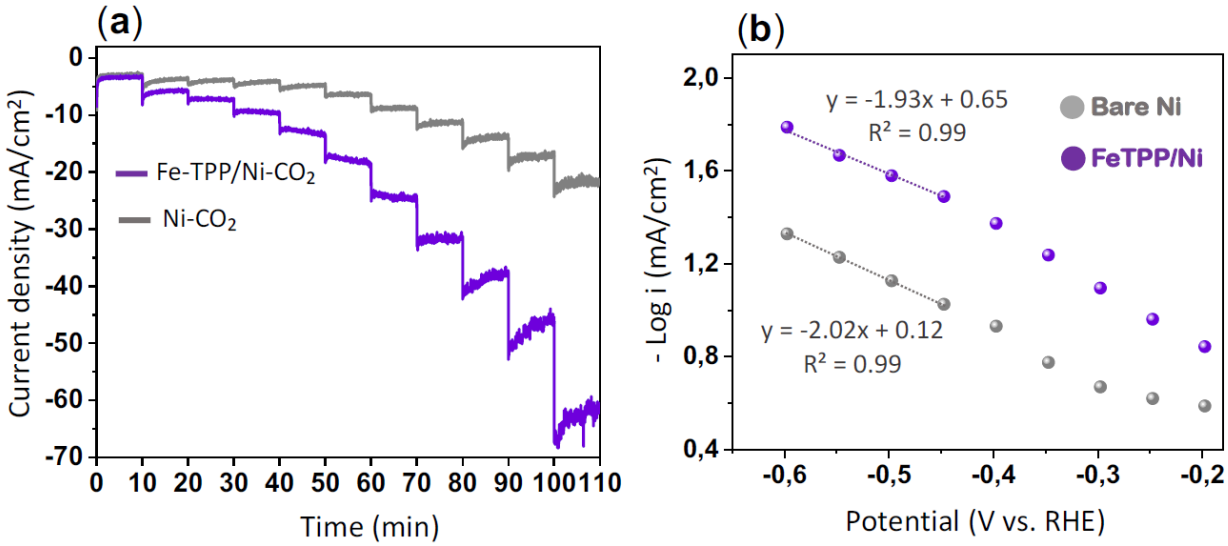

Fig. S44. (a) Tafel plot for the 3D nickel electrode (black) and the 3D nickel electrode loaded with Fe-TPP (purple) in 0.5 M $KHCO_3$; (b) Tafel slope comparison of bare Ni and Fe-TPP/Ni.

Figure S44 Additional Text: Tafel slopes and electrochemical surface area (ECSA) were calculated to obtain additional insight into the reaction kinetics of each individual bare Ni and Fe-TPP/Ni catalyst towards the CO_2RR. Tafel analyses show a significantly higher exchange current and slightly lower slope for Fe-TPP/Ni compared to bare Ni. This suggests that the rate-determining step for ethanol formation may change with the Fe-TPP catalyst.[19–21] The temperature was measured and compared under Ar and CO_2 for the entire reaction, which shows a slight rise along with increasing the potential energy (Fig. S44). The cell is operated with no electrolyte flow and a CO_2 flow rate of 40 sccm respectively. Each set potential is held for 10 minutes in order to allow for the current to stabilize. Tafel analyses comparison for electrocatalytic CO_2RR to ethanol on bare nickel and Fe-TPP/Ni, show a lower slope in the case of Fe-TPP/Ni. This suggests that the rate-determining step for ethanol formation may change with the Fe-TPP catalyst.[19–21]

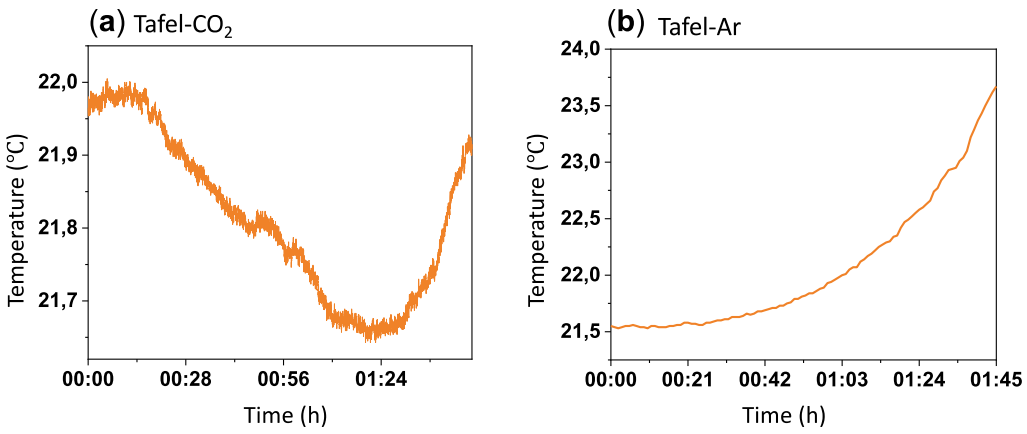

Fig. S45. Temperature control during Tafel plot under (a) CO_2 and (b) Ar.

Electrochemically Active Surface Area (ECSA)

ECSA of the bare nickel electrode and Fe-TPP/Ni was determined from the electrochemical double–layer capacitance (Fig. S46).[22] Comparing the results, the ECSA of Fe-TPP/Ni is 1.5 fold larger than the ECSA of bare Ni. This could be due to the additional conductive molecular layer within the pores of the nickel electrode increasing the electrochemically active surface area. It was determined from the electrochemical double–layer capacitance [22,23]. First, a potential window between 0.1 V and 0.2 V vs. RHE was identified via cyclic voltammetry in which little to no faradaic currents occur. Within this window, cyclic voltammograms at increasing scan rates are measured including a 10 s hold at each potential vertex. The resulting charging currents, I^+ and I^-, are measured at 0.15 V vs RHE for both the positive and negative sweeps, respectively. These are related to the scan rate ν and the double layer capacitance C_{DL} as follows [22,24,25]:

$$I^{+/-} = \nu C_{DL}^{+/-} \qquad \text{(Eq. 6)}$$

The slope of the capacitive current vs. the scan rate constitutes the double layer capacitance and can be determined from a linear fit of the experimental data (Fig S49 (c)). It is common practice to report the average double layer capacitance $\overline{C_{DL}}$ which is determined from the average of the absolute values of both the positive and negative potential sweeps [22,26].

$$\overline{C_{DL}} = \frac{C_{DL}^{+} + |C_{DL}^{-}|}{2} \qquad \text{(Eq.7)}$$

The ECSA can then be estimated from the specific capacitance of the sample, C_s [22]:

$$ECSA = \frac{\overline{C_{DL}}}{C_s} \qquad \text{(Eq.8)}$$

The specific capacitance C_s represents the capacitance per unit area of an ideally smooth surface of the studied material paired with an electrolyte. Technically, C_s has to be determined

experimentally for each catalyst and electrolyte condition. While specific capacitances have been measured for nickel in various NaOH and KOH solutions, these values vary significantly depending on the electrolyte composition and concentration [22]. Moreover, to the best of our knowledge, there are no measurements of C_s available for the here discussed Fe-TPP. This is further exacerbated by the presence of dissolved CO_2, which warrants additional measurements of C_s specifically for the presented application. Overall, the double-layer capacitance increases from 136 mF before Fe-TPP loading to 194.5 mF following the loading procedure (≈ + 43 %).

To arrive at an estimate for the roughness factor R and the volume specific surface area a_V of the sintered 3D nickel electrode, we use the average value of 40 $\mu F/cm^2$ reported by McCrory for alkaline solutions [22]. According to eq. 7., this results in an electrochemically active surface area of 3402 $cm^2$and 4850 cm^2 before and after Fe-TPP loading, respectively. The roughness factor R for the nickel electrode loaded with Fe-TPP is determined as the ratio of the electrochemically active surface area over the geometric surface area $A_{tot,}$ 3D which is calculated from the adjusted CAD model:

$$R = \frac{ECSA}{A_{tot,3D}} = \frac{4850\ cm^2}{40.49\ cm^2} = 119.78 \qquad \text{(Eq.9)}$$

The volume specific surface area a_V is defined as the electrochemically active surface area over the porous electrode volume which constitutes the pore volume V_p and the solid nickel volume V_{Ni} (see eq. 1):

$$a_V = \frac{ECSA}{V_P + V_{Ni}} = \frac{ECSA}{\frac{m_{H2O}}{\rho_{H2O}} + \frac{m_{Ni}}{\rho_{Ni}}} = \frac{4850\ cm^2}{1.531\ cm^3} = 3167.86\ \frac{cm^2}{cm^3}\ (\approx 3.17\ x\ 10^5\ \frac{m^2}{m^3}) \qquad \text{(Eq.10)}$$

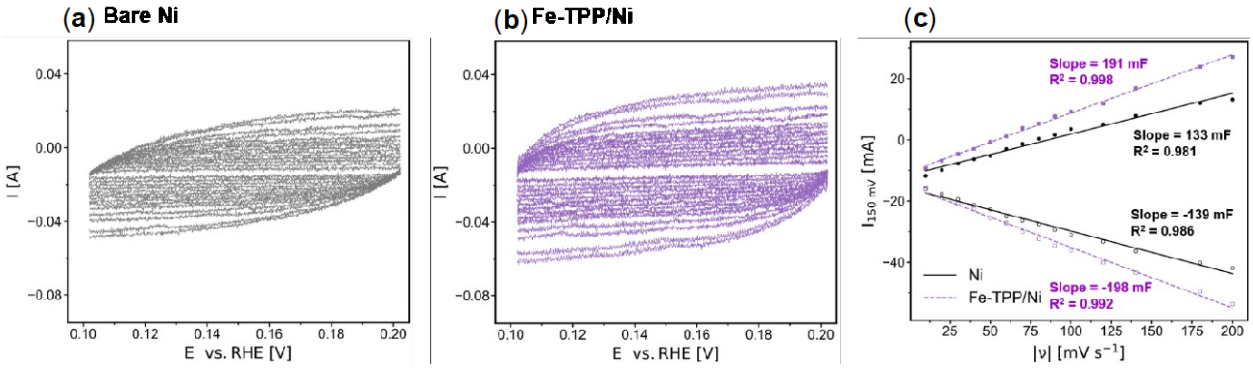

Fig. S46. Cyclic voltammograms in 0.5 M $KHCO_3$ with varying scan rates in a non-Faradaic potential region in order to estimate the electrochemically active surface area (ECSA) for a bare nickel electrode (A) and a nickel electrode loaded with Fe-TPP (B). (C) The double-layer capacitance C_{DL} is estimated from the slope of the anodic (Ni: ●, Fe-TPP/Ni: ■) and the cathodic (Ni: ○, Fe-TPP/Ni: □) double-layer charging current measured at 0.15 V vs RHE vs. the scan rate. Scan rates of 10, 20, 30, 40, 50, 60, 70, 80, 90, 120, 140, 180 and 200 mV/s are applied between 0.1 V and 0.2 V vs. RHE.

SI References

1. Liu, T. *et al.* Interfacial Electron Transfer of Ni2P–NiP2 Polymorphs Inducing Enhanced Electrochemical Properties. *Adv. Mater.* **30**, 1803590 (2018).
2. Liu, C. *et al.* Binary nickel iron phosphide composites with oxidized surface groups as efficient electrocatalysts for the oxygen evolution reaction. *Sustain. Energy Fuels* **3**, 3518–3524 (2019).
3. Zhang, J. *et al.* Hybrid Ni(OH)2/FeOOH@NiFe Nanosheet Catalysts toward Highly Efficient Oxygen Evolution Reaction with Ultralong Stability over 1000 Hours. *ACS Sustain. Chem. Eng.* **7**, 14601–14610 (2019).
4. Zhou, Y., Li, J., Wang, S., Zhang, J. & Kang, Z. From MOF membrane to 3D electrode: a new approach toward an electrochemical non-enzymatic glucose biosensor. *J. Mater. Sci.* **52**, 12089–12097 (2017).
5. Gao, S., Liao, F., Ma, S., Zhu, L. & Shao, M. Network-like mesoporous NiCo2O4 grown on carbon cloth for high-performance pseudocapacitors. *J. Mater. Chem. A* **3**, 16520–16527 (2015).
6. Buchner, F. *et al.* Coordination of Iron Atoms by Tetraphenylporphyrin Monolayers and Multilayers on Ag(111) and Formation of Iron-Tetraphenylporphyrin. *J. Phys. Chem. C* **112**, 15458–15465 (2008).
7. Gottfried, J. M., Flechtner, K., Kretschmann, A., Lukasczyk, T. & Steinrück, H.-P. Direct Synthesis of a Metalloporphyrin Complex on a Surface. *J. Am. Chem. Soc.* **128**, 5644–5645 (2006).
8. Atkins, P. *Chemical Principles*. (W.H. Freeman and Company, 2013).
9. Liu, X. *et al.* Understanding trends in electrochemical carbon dioxide reduction rates. *Nat. Commun.* **8**, 15438 (2017).
10. Montoya, J. H., Shi, C., Chan, K. & Nørskov, J. K. Theoretical Insights into a CO Dimerization Mechanism in CO2 Electroreduction. *J. Phys. Chem. Lett.* **6**, 2032–2037 (2015).
11. Pérez-Gallent, E., Figueiredo, M. C., Calle-Vallejo, F. & Koper, M. T. M. Spectroscopic Observation of a Hydrogenated CO Dimer Intermediate During CO Reduction on Cu(100) Electrodes. *Angew. Chemie Int. Ed.* **56**, 3621–3624 (2017).
12. Schouten, K. J. P., Qin, Z., Pérez Gallent, E. & Koper, M. T. M. Two Pathways for the Formation of Ethylene in CO Reduction on Single-Crystal Copper Electrodes. *J. Am. Chem. Soc.* **134**, 9864–9867 (2012).
13. Arán-Ais, R. M., Gao, D. & Roldan Cuenya, B. Structure- and Electrolyte-Sensitivity in CO2 Electroreduction. *Acc. Chem. Res.* **51**, 2906–2917 (2018).
14. Shen, J., Kolb, M. J., Göttle, A. J. & Koper, M. T. M. DFT Study on the Mechanism of the Electrochemical Reduction of CO2 Catalyzed by Cobalt Porphyrins. *J. Phys. Chem. C* **120**, 15714–15721 (2016).
15. Li, F. *et al.* Cooperative CO2-to-ethanol conversion via enriched intermediates at molecule–metal catalyst interfaces. *Nat. Catal.* **3**, 75–82 (2020).
16. Okada, S. & Segawa, H. Substituent-Control Exciton in J-Aggregates of Protonated Water-Insoluble Porphyrins. *J. Am. Chem. Soc.* **125**, 2792–2796 (2003).
17. Yamaguchi, T., Kimura, T., Matsuda, H. & Aida, T. Macroscopic Spinning Chirality Memorized in Spin-Coated Films of Spatially Designed Dendritic Zinc Porphyrin J-Aggregates. *Angew. Chemie Int. Ed.* **43**, 6350–6355 (2004).
18. Helmli, F. Focus Variation Instruments BT - Optical Measurement of Surface Topography. in (ed. Leach, R.) 131–166 (Springer Berlin Heidelberg, 2011).
19. Dinh, C. T. *et al.* CO2electroreduction to ethylene via hydroxide-mediated copper catalysis at an abrupt interface. *Science (80-.).* **360**, 783–787 (2018).
20. Gao, S. *et al.* Partially oxidized atomic cobalt layers for carbon dioxide electroreduction to liquid fuel. *Nature* **529**, 68–71 (2016).
21. Ma, W. *et al.* Electrocatalytic reduction of CO2 to ethylene and ethanol through hydrogen-assisted

C–C coupling over fluorine-modified copper. *Nat. Catal.* **3**, 478–487 (2020).
22. McCrory, C. C. L., Jung, S., Peters, J. C. & Jaramillo, T. F. Benchmarking heterogeneous electrocatalysts for the oxygen evolution reaction. *J. Am. Chem. Soc.* **135**, 16977–16987 (2013).
23. Trasatti, S. & Petrii, O. A. Real surface area measurements in electrochemistry. *Pure Appl. Chem.* **63**, 711–734 (1991).
24. Connor, P., Schuch, J., Kaiser, B. & Jaegermann, W. The Determination of Electrochemical Active Surface Area and Specific Capacity Revisited for the System MnOx as an Oxygen Evolution Catalyst. *Zeitschrift fur Phys. Chemie* **234**, 979–994 (2020).
25. Zankowski, S. P. & Vereecken, P. M. Electrochemical Determination of Porosity and Surface Area of Thin Films of Interconnected Nickel Nanowires. *J. Electrochem. Soc.* **166**, D227–D235 (2019).
26. Kou, T. *et al.* Periodic Porous 3D Electrodes Mitigate Gas Bubble Traffic during Alkaline Water Electrolysis at High Current Densities. *Adv. Energy Mater.* **2002955**, 1–11 (2020).